

1 **Radiative and Thermodynamic Responses to Aerosol Extinction Profiles during the**
2 **Pre-monsoon Month over South Asia**

3

4 Y. Feng^{1*}, V. R. Kotamarthi¹, R. Coulter¹, C. Zhao², and M. Cadetdu¹

5

6 ¹Environmental Science Division, Argonne National Laboratory, Argonne, IL

7 ²Atmospheric Science and Global Change Division, Pacific Northwest National Laboratory,

8 Richland, WA

9 *e-mail: yfeng@anl.gov

10 **Abstract.** Aerosol radiative effects and thermodynamic responses over South Asia are
11 examined with the Weather Research and Forecasting model coupled with Chemistry
12 (WRF-Chem) for March 2012. Model results of Aerosol Optical Depths (AOD) and
13 extinction profiles are analyzed and compared to satellite retrievals and two ground-based
14 lidars located in the northern India. The WRF-Chem model is found to heavily underestimate
15 the AOD during the simulated pre-monsoon month and about 83% of the model low-bias is
16 due to aerosol extinctions below ~2 km. Doubling the calculated aerosol extinctions below
17 850 hPa generates much better agreement with the observed AOD and extinction profiles
18 averaged over South Asia. To separate the effect of absorption and scattering properties, two
19 runs were conducted: in one run (Case I), the calculated scattering and absorption coefficients
20 were increased proportionally, while in the second run (Case II) only the calculated aerosol
21 scattering coefficient was increased. With the same AOD and extinction profiles, the two runs
22 produce significantly different radiative effects over land and oceans. On the regional mean
23 basis, Case I generates 48% more heating in the atmosphere and 21% more dimming at the
24 surface than Case II. Case I also produces stronger cooling responses over the land from the
25 longwave radiation adjustment and boundary layer mixing. These rapid adjustments offset the
26 stronger radiative heating in Case I and lead to an overall lower-troposphere cooling up to
27 -0.7 K day^{-1} , which is smaller than that in Case II. Over the ocean, direct radiative effects
28 dominate the heating rate changes in the lower atmosphere lacking such surface and lower
29 atmosphere adjustments due to fixed sea surface temperature, and the strongest atmospheric
30 warming is obtained in Case I. Consequently, atmospheric dynamics (boundary layer heights
31 and meridional circulation) and thermodynamic processes (water vapor and cloudiness) are
32 shown to respond differently between Case I and Case II underlying the importance of
33 determining the exact portion of scattering or absorbing aerosols that lead to the
34 underestimation of aerosol optical depth in the model. In addition, the model results suggest
35 that both direct radiative effect and rapid thermodynamic responses need to be quantified for
36 understanding aerosol radiative impacts.

37

38 **1. Introduction**

39 South Asia, including the Indian subcontinent and adjacent oceans, is a regional hotspot
40 with high aerosol loadings (Ramanathan et al., 2001; Moorthy et al., 2013). Aerosols over
41 this region are composed of locally emitted sulfate, black carbon (BC), and organic
42 substances (mainly from industrial, transportation, residential, and agricultural burning), as
43 well as long-range-transported desert dust and sea spray aerosols. These aerosols together
44 induce a large negative radiative forcing at the top of the atmosphere (TOA) through direct
45 scattering and absorption of incoming solar radiation. With year 2000 emissions, Chung et al.
46 (2010) estimated the regional TOA aerosol forcing in South Asia at about -1.9 W m^{-2} , which
47 is larger by several factors than the present-day global mean direct forcing (Boucher et al.,
48 2013). The overall aerosol cooling effect in response to negative TOA forcing is suggested to
49 weaken the sea surface temperature gradient over the Indian Ocean and decelerate the
50 monsoonal circulation and moisture transport (Ramanathan et al., 2005). Other studies show
51 that local warming by BC in the upper troposphere intensifies vertical motion over land and
52 modulates intraseasonal monsoon rainfall variations (Lau et al., 2006). Therefore, rapidly
53 increased anthropogenic aerosol emissions in South Asia have been linked closely to
54 observed changes in surface temperature and rainfall patterns in global climate simulations
55 (Meehl et al., 2008; Lau et al., 2009; Wang et al., 2009; Bollasina et al., 2011; Ganguly et al.,
56 2012).

57 For quantifying aerosol direct perturbations in the radiation budget, column-integrated
58 aerosol optical depth (AOD) is often examined in global models, some of which include
59 regional analysis over South Asia (Myhre et al., 2009, 2013; Shindell et al., 2013; Boucher et
60 al., 2013; Pan et al., 2015), and in regional-scale models (Chung et al., 2010; Nair et al., 2012;
61 Kumar et al., 2014). Besides AOD, aerosol single scattering albedo (SSA) has also been
62 identified as a main source of uncertainty in estimates of aerosol direct forcing (McComiskey
63 et al., 2008; Loeb and Su et al., 2010) and evaluated with observations. Most models
64 underpredict aerosol abundances over South Asia versus data from the ground-based Aerosol
65 Robotic Network (AERONET) (Holben et al., 1998) or satellite-retrieved AOD observations
66 such as the Moderate Resolution Imaging Spectroradiometer (MODIS) (e.g., Yu et al., 2003;
67 Kinne et al., 2006; Koch et al., 2009; Ganguly et al., 2012). In addition, models also tend to

68 underestimate aerosol absorption by over-estimating the SSA (Liu et al., 2012). Such low
69 biases in aerosol optical properties might potentially affect model simulations of regional
70 climatology and assessment of aerosol climate impacts over the South Asia region.

71 Vertical distribution of aerosols is another important parameter in determining
72 aerosol-radiation interactions. When column AOD is constrained, uncertainties in aerosol
73 vertical profiles can still contribute to significant uncertainties in the calculation of radiative
74 forcing (Lohmann et al., 2001; Zarzycki and Bond, 2010; Ban-Weiss et al., 2011). The extent
75 to which the aerosol profile impacts aerosol radiative effects depends on the presence of
76 cloud, surface albedo, and SSA. Column and global aerosol and radiation models have been
77 used to explore the sensitivity of aerosol direct radiative forcing to the vertical distribution of
78 aerosols, especially absorbing aerosols, relative to clouds (Haywood and Shine, 1997; Liao
79 and Seinfeld, 1998; Samset et al., 2013; Vuolo et al., 2014; Choi and Chung, 2014). However,
80 compared to column AOD and SSA, aerosol vertical distributions are evaluated less
81 frequently against observations, partly due to lack of observational data sets.

82 Aircraft profiling of aerosol concentrations from recent airborne experiments, such as the
83 HIAPER Pole-to-Pole Observations (Schwarz et al., 2010) and the Arctic Research of the
84 Composition of the Troposphere from Aircraft and Satellites (Jacob et al., 2010), provides
85 high-quality data sets for model comparison (e.g., Koch et al, 2009; Liu et al., 2012).
86 However, these data sets are usually available only for limited locations and time periods. In
87 particular, few long-term aircraft surveys are available for South Asia, other than a few past
88 field experiments such as the Maldives Autonomous Unmanned Aerial Vehicle Campaign
89 (Ramanathan et al., 2007) and the Integrated Campaign for Aerosol, Gases and Radiation
90 Budget experiment (Satheesh et al., 2009). Satellite-retrieved aerosol extinction profiles
91 providing wide coverage in space and time have been used increasingly for model evaluation.
92 Using the Cloud-Aerosol Lidar and Infrared Pathfinder Satellite Observations (CALIPSO)
93 lidar nighttime data at 532 nm in cloud-free conditions from June 2006 to November 2007,
94 Yu et al. (2010) evaluated aerosol extinction profiles simulated by the Goddard Chemistry
95 Aerosol Radiation Transport (GOCART) model and found substantial underestimation in the
96 magnitude of aerosol extinctions over the Indian subcontinent. Similar analysis of all-sky
97 CALIPSO nighttime data in the AeroCom (Aerosol Comparisons between Observations and

98 Models) multi-model evaluation of the vertical distribution of aerosols (Koffi et al., 2012)
99 found that 11 of the 12 AeroCom models underestimated the annual mean aerosol extinctions
100 below 2 km over South Asia. A recent study by Quennehen et al. (2015) examined six global
101 and one regional models with CALIPSO-derived backscatter profiles at 532nm during August
102 and September 2008, and the multi-model mean backscatter is also underestimated between 0
103 and 2 km over northern India and eastern China.

104 Although these model-data comparisons help to identify the biases in model simulations
105 of aerosol extinction or concentration profiles, the resultant changes in atmospheric heating,
106 dynamics, and cloud adjustments (the aerosol semi-direct effects) have yet to be investigated.
107 Moreover, satellite retrievals of aerosol extinction profiles are also subject to uncertainties
108 associated with cloud contamination, surface overlap correction, and daylight background
109 noise. Observational studies have examined atmospheric heating rates extensively by using
110 aerosol extinctions retrieved from ground-based or CALIPSO lidar instruments (Misra et al.,
111 2012; Gautam et al., 2010; Kuhlmann and Quaas, 2010) and *in situ* aircraft data (Ramana et
112 al., 2007; Satheesh et al., 2008). These studies directly provide observational constraints on
113 the instantaneous atmospheric heating caused by aerosols, ranging from 0.35 to 2 K day⁻¹, in
114 the South Asia region. On the other hand, observational methods face challenges in
115 distinguishing the rapid adjustments in the atmosphere attributable to aerosols versus other
116 environmental influences.

117 In the present study, we examine the atmospheric radiative and thermodynamic responses
118 to uncertainty associated with vertical distributions of aerosol extinction coefficient by
119 correcting bias in model calculations with satellite and surface remote sensing data. This not
120 only identifies discrepancies between the model-predicted and observed aerosol optical
121 properties as a function of height, but it also demonstrates the potential importance of
122 aerosol-related uncertainty for regional climate simulations. The regional Weather Research
123 and Forecasting (WRF) model, coupled with a chemistry module (WRF-Chem), is used to
124 simulate the pre-monsoon month of March 2012 over South Asia. The next section describes
125 the regional climate model configurations and ground-based and satellite data sets available.
126 Section 3 evaluates the modeled and observed AODs and aerosol profiles and discusses
127 changes in the simulated radiative energy balance, surface temperature, lower-atmospheric

128 heating rates, boundary layer (BL) height, large-scale circulation, and cloud occurrence, in
129 response to optimized matching of aerosol extinction profiles to observations. The main
130 findings of this study and implications for future work are summarized in Section 4.

131 **2. Methodology**

132 **2.1 Model description**

133 This study uses a version of the WRF-Chem 3.3 (Skamarock et al., 2008; Grell et al.,
134 2005), coupled with the chemistry module MOZCART (Pfister et al., 2011), to simulate
135 aerosol distributions, aerosol-radiation interactions, and regional meteorological fields. The
136 default model simulations are performed for eight months from August 2011 to March 2012,
137 the period when multi-instrumental aerosol observations were collected by the U.S.
138 Department of Energy (DOE) Ganges Valley Aerosol Experiment (GVAX) at a mountain-top
139 site, Nainital (29°N, 79°E, e.s.l. 1939 m), in northern India. The model domain is configured
140 from 55°E to 95°E and 0° to 36°N, with a horizontal grid spacing of ~12 km and 27 vertical
141 layers. The MOZCART chemistry module (WRF-Chem Version 3.7 User's guide: [http://](http://ruc.noaa.gov/wrf/WG11/Users_guide.pdf)
142 http://ruc.noaa.gov/wrf/WG11/Users_guide.pdf) includes the MOZART-4 gas-phase
143 chemistry (Emmons et al., 2010) and the GOCART bulk aerosol scheme (Chin et al., 2002).
144 MOZCART simulates externally mixed aerosol species including sulfate, BC, organic carbon
145 (OC), dust (in 5 size bins with 0.5, 1.4, 2.4, 4.5, and 8 μm effective radius) and sea salt (in 4
146 size bins with 0.3, 1.0, 3.2, and 7.5 μm effective radius). This version of the WRF-Chem
147 aerosol and chemistry modules has been used and evaluated in studying effects of dust
148 aerosols on tropospheric chemistry during the pre-monsoon season in northern India (Kumar
149 et al., 2014).

150 The anthropogenic emissions of gaseous species are derived from the Reanalysis of the
151 Tropospheric Chemical Composition and Emissions Database for Global Atmospheric
152 Research compiled for the year 2000. The default emissions of BC, OC, and SO₂ are same as
153 in the GOCART model for year 2006. Over India, emissions of BC, OC, and SO₂ are
154 replaced with year 2010 inventories available at resolutions of 0.1° × 0.1° for anthropogenic
155 sources and 0.5° × 0.5° for biomass burning (Lu et al., 2011). The total emissions of BC and
156 OC used in this study are about 1.12 Gg/yr and 3.06 Gg/yr over India, respectively, roughly
157 51% and 63% higher than those from the default GOCART global inventories (0.74 Gg/yr

158 and 1.88 Gg/yr). The total SO₂ emissions in South Asia with updated emissions over India
159 are 9.36 Gg yr⁻¹, slightly less than the default GOCART emissions (10 Gg yr⁻¹). Additional
160 sulfate emissions from waste and biofuel burning (Yevich and Logan, 2003) are also included
161 (about 0.21 Gg/yr). Dimethyl sulfide, dust, and sea salt emissions are calculated online as for
162 the GOCART model (Ginoux et al., 2001; Chin et al., 2002). Primary aerosol emissions
163 including all the anthropogenic, biomass burning and natural sources are injected into the
164 lowest level of the model and transported by advection and updrafts. Calculations of optical
165 properties of aerosols assume internal mixing (Fast et al., 2006) including the Kappa-based
166 hygroscopic growth of aerosol components (Petters and Kreidenweis, 2007), although
167 aerosols are transported as external mixtures. The Rapid Radiative Transfer Model for
168 General Circulation Model schemes (Iacono et al., 2008) is used for shortwave and longwave
169 radiation calculations (Zhao et al., 2011). Other main physical packages used in this study are
170 the Thompson cloud microphysics (Thompson et al., 2008), the Zhang-McFarlane cumulus
171 parameterization (Zhang and McFarlane, 1995), the Mellor-Yamada-Janjic BL scheme (Janjic,
172 1994), and the Rapid Update Cycle land surface model (Benjamin et al., 2004).

173 The initial and boundary conditions of meteorological fields were interpolated to the
174 model time step (72 s) from the compiled 6-h National Centers for Environmental Prediction
175 reanalysis data available at 1° × 1° resolution. Outputs from the MOZART-4 global chemical
176 transport model (Emmons et al., 2010) generated for the simulation time periods are used for
177 chemistry initial and boundary conditions. Radiative feedbacks of aerosols are coupled with
178 the meteorology updates at each model time step. Indirect aerosol microphysical effects are
179 not considered. While this omission might affect the simulated total aerosol radiative impact,
180 the focus here is on examination of the model's sensitivity to uncertainty in predicted aerosol
181 extinction, which, as an aerosol optical property, has a direct impact on aerosol direct and
182 semi-direct radiative effects more than aerosol microphysical effect.

183 The model-data analysis and discussions here center on simulations in March 2012, for
184 two reasons. First, during this pre-monsoon month, ground-based lidar measurements are
185 available at Nainital and Kanpur (in northern India) and used with satellite observations to
186 characterize bias in the calculated aerosol extinctions. As discussed later, it is important to
187 have independently calibrated ground-based measurements because of the uncertainty

188 associated with satellite data. Second, we examine the model's performance in simulating
189 AOD and vertical distributions for this pre-monsoon month, because the anthropogenic
190 aerosol concentrations over this period are among the highest of the year and impose large
191 radiative forcing (Ramanathan et al., 2007). Uncertainty in aerosol predictions might
192 propagate into the predicted meteorological fields and influence the moisture distribution in
193 the pre-monsoon-to-monsoon season. In addition to the default (control) run for March, two
194 sensitivity model simulations are conducted with corrected extinction profiles, as described
195 below. One-week spin-up is used for initializing the one-month runs.

196 **2.2 Observational data sets**

197 During the GVAX experiment, the DOE Atmospheric Radiation Measurements (ARM)
198 Program Mobile Facility 1 (AMF-1) was operated at Nainital in the central Himalayan region
199 of the northern India. Located at ~1939 m above sea level, this site was frequently near the
200 planetary BL top or in the free troposphere during the experimental period. Ground-based
201 AMF-1 multi-filter rotating shadowband radiometer (MFRSR) measurements were made
202 from September 2011 to March 2012. The post-processed, quality-assured AOD products
203 (pghmfrsraod1michM1.s1) from the MFRSR are used to evaluate the model simulations of
204 monthly and daily mean daytime (0600-1800 local time) AODs. Instrumental uncertainty in
205 the MFRSR-retrieved AOD is about 0.026 above 380 nm (Schmid et al., 1999), which is
206 generally below the typical AOD levels observed at this site. Monthly mean AERONET
207 (Holben et al., 1998) level 2 sun photometer AOD data sets that are also used have a reported
208 uncertainty of approximately 0.01 at 500 nm (Eck et al., 1999; Smirnov et al., 2000).
209 Comparisons of the simulated monthly mean AODs with Moderate Resolution Imaging
210 Spectroradiometer (MODIS)/Terra satellite observations (MOD08 Level 3, edition 5; Platnick
211 et al., 2003) are used to evaluate the geographic distribution of AOD.

212 Vertical profiles of aerosol extinction at 532 nm are retrieved at Nainital from micropulse
213 lidar (MPL) backscatter measurements and MFRSR AOD data for March 2012, according to
214 Kafle and Coulter (2013) and Klett (1981). After exclusion of cloud contamination and
215 missing data, 26 days of MPL-retrieved extinction profiles remain, 25 of which have valid
216 data during the daytime when MFRSR AOD retrievals are available. The 30-min-frequency
217 extinction retrievals are averaged hourly and monthly for model comparison with a vertical

218 resolution of ~500 m. Aerosol extinction profiles at 532 nm are also available at a nearby
219 low-elevation site, Kanpur (26.5°N, 80.3°E, e.s.l. 120m), from the National Aeronautics and
220 Space Administration's MPL network (MPLNET; Welton et al., 2001). Unlike Nainital,
221 which is located near the BL top, the Kanpur site provides aerosol characteristics close to the
222 surface pollution sources in the Indo-Gangetic Basin. During winter and the pre-monsoon
223 season, this site is often loaded with high concentrations of anthropogenic aerosols mixed
224 with dust from episodic events (Dey and Di Girolamo, 2010). The quality-assured MPLNET
225 level 2 daytime products are available from August 2011 to March 2012 for model
226 comparison. In addition to the ground-based remote sensing data, CALIPSO satellite
227 retrievals of extinction profiles from the Cloud–Aerosol Lidar with Orthogonal Polarization
228 sensor (Winker et al., 2009), version 3, level 2, nighttime products are also used to
229 characterize regional variations in aerosol vertical distribution. Uncertainties associated with
230 these lidar retrievals of aerosol extinction profiles, either space-borne or ground-based,
231 include overlapping corrections near the surface, signal-to-noise ratio in the background
232 (Welton and Campbell, 2002), and propagated errors in AOD measurements (Kafle and
233 Coulter, 2013). The observations of extinction profiles are used mainly to identify and correct
234 systematic bias in the model-simulated monthly mean vertical profiles of aerosols. The
235 aerosol abundances in the column are constrained with column-integrated AOD
236 measurements from MFRSR and MODIS.

237 **3. Results**

238 **3.1 Aerosol optical depth**

239 The model simulations of monthly mean AOD for March 2012 are compared with the
240 MODIS/Terra satellite observations in Fig. 1. During this time of the year, the Indo-Ganges
241 Valley is impacted with locally emitted aerosols from urban and industrial sources as well as
242 dust mainly from nearby arid agricultural lands and deserts (Giles et al., 2011). As shown in
243 Fig. 1a, the MODIS retrievals of AOD are generally larger than 0.5 in these areas. Given the
244 dry pre-monsoon conditions with small wet removal, these aerosols are transported in long
245 distance by the northwesterly winds prevailing in the Valley. That leads to similarly high
246 AODs (>0.5) over to the Bay of Bengal and the eastern India in the MODIS observations.
247 Another aerosol hotspot is off the southwest coast of the Indian subcontinent, influenced by

248 both nearby anthropogenic emissions in the western India and long-range transported
249 pollutions from the northern India (Ramanathan et al., 2001). Dust dominates the AOD
250 observed over the Arabian Sea with values about 0.3~0.5.

251 The model-calculated AODs (shown in Fig. 1b) are lower than MODIS retrievals over
252 most of the domain, while the overall geographic pattern of AOD distributions is simulated
253 except for over the Arabian Sea. Large AODs are predicted in northern and eastern India and
254 along the pathway that the aerosol plumes travel to southwestern India and the downwind as
255 depicted similarly in the MODIS observations. But the maximum AOD values calculated by
256 the model are much lower around 0.3~0.4. AODs less than 0.1 are predicted over most of
257 northwestern India and the adjacent oceans, whereas MODIS has much higher values (> 0.3).
258 These discrepancies could be attributable to episodic dust activities not reproduced by
259 WRF-Chem (as shown in Fig. S1 in the Supplement that dust aerosols are dominating species)
260 or to overestimation associated with the MODIS satellite retrievals over highly reflective
261 surfaces such as deserts and clouds over the ocean. In other aerosol-concentrated regions,
262 anthropogenic pollutants such as sulfate, BC, and OC are the main contributors to the AOD
263 underestimation (Fig. S1).

264 The degree to which the model-calculated AOD is lower than the MODIS data is further
265 shown in Fig. 1c for March 2012. The figure compares the latitudinal variations in AOD
266 averaged between 60°E and 95°E. The default model (control run) calculations of AOD are
267 systematically smaller than the MODIS data (by about a factor of 2), from the Equator
268 northward to 27°N (Latitudes north of 27°N are not shown for the MODIS data, because
269 more than 2/3 of the data are missing). Despite the underestimation in absolute AODs, a
270 gradient in AOD calculated as a function of latitude is similar to the MODIS observations,
271 increasing by about ~0.1 AOD every 10° in latitude. In addition, the calculated daily daytime
272 mean AODs are compared in Fig. 1d with ground-based GVAX MFRSR measurements at
273 Nainital and AERONET data at nearby Kanpur (~390 km southeast; locations of the two sites
274 are marked in Fig. 1b). Being a relatively clean site, Nainital has a monthly mean AOD of
275 0.232 from MFRSR measurements, while the mean AERONET AOD is 0.583 at Kanpur. The
276 discrepancies between the modeled and observed AOD are much smaller at the Nainital site.
277 The monthly mean AOD at Nainital is estimated at 0.181 by WRF-Chem — about 22% lower

278 than the MFRSR AOD — and the model-data difference is only 13% if the outlier on day 27
279 of the observations is excluded. In contrast, the model’s underestimation at Kanpur is about
280 54%, which is more close to the zonal-mean differences shown in Fig. 1c. These differences
281 in AOD comparison imply that WRF-Chem tends to underpredict aerosol extinction (whose
282 vertical integral is AOD) at lower elevations (in the BL) more than in the free troposphere
283 over this region, as the Nainital data are more representative of the atmosphere near or above
284 the BL top.

285 Similar underestimation in the modeled AOD compared with the MODIS observations is
286 also found for other months between August 2011 and March 2012 (Fig. S2 in the
287 Supplement). The AOD underestimation is one of the common problems in aerosol model
288 simulations for post-monsoon and winter time periods over the S Asian region. Pan et al.
289 (2015) suggested several possible causes including suppression of the aerosol hygroscopic
290 growth and formation of secondary inorganic aerosol due to low-biased relative humidity in
291 the boundary layer (Feng et al., 2015), omission of nitrate aerosol, and underestimated
292 emissions from agricultural waste burning and biofuel usage. Resolving these differences in
293 AOD is beyond the scope of this paper that intends to identify the vertical location of the
294 AOD biases and investigate the subsequent responses, but certainly deserves further
295 investigation.

296 **3.2 Aerosol extinction profiles**

297 To further evaluate the vertical distribution of calculated aerosol extinctions (b_{ext}), the
298 ground-based MPL retrievals available in March 2012 at Nainital and Kanpur, along with
299 CALIPSO satellite retrievals, are used. Figure 2 compares the simulated monthly mean
300 vertical profiles of b_{ext} with the observational data sets. Like column-integrated AOD,
301 calculated aerosol extinctions are also lower at the high-elevation Nainital site (Fig. 2a), at
302 the polluted surface Kanpur site (Fig. 2b), and as an average over the South Asia region (Fig.
303 2c). Moreover, the discrepancies between the modeled and observed profiles are larger in the
304 lower atmosphere, where aerosols are more concentrated (as indicated by larger extinctions),
305 than at higher altitudes in the free troposphere. These differences are further illustrated in Fig.
306 2d-f, which shows the percent differences in calculated extinction profiles relative to the
307 CALIPSO data in the column. Table 1 summarizes the column-mean relative differences (%)

308 between the predicted monthly mean b_{ext} and retrievals from the CALIPSO data, expressed
 309 as

$$\frac{\sum_{i=1}^n \frac{[b_{ext,model}(i) - b_{ext,CALIPSO}(i)]}{b_{ext,CALIPSO}(i)}}{n} \times 100, \quad (1)$$

310 where $b_{ext,CALIPSO} > 0.01$, and i denotes the vertical levels from the surface up to 8 km
 311 (level n) at 0.1 km intervals. For altitudes below 850 hPa (or ~2-3 km, depending on the
 312 location), the calculated average differences between the model control run and the
 313 CALIPSO data are -56%, -52%, and -77% for Nainital, Kanpur, and South Asia, respectively.
 314 In comparison, smaller differences of -33%, -33%, and -75%, respectively, are estimated for
 315 the entire column.

316 The monthly mean extinction height (z_{α}), defined as $\frac{\sum_{i=1}^n b_{ext,i} z_i}{\sum_{i=1}^n b_{ext,i}}$ (Koffi et al., 2012), is
 317 also calculated in order to compare the modeled aerosol mean vertical structure with
 318 observations (Table 2). On a regional mean basis over South Asia, z_{α} estimated from the
 319 March CALIPSO data is 1.7 km in this study. This value is consistent with the
 320 March-April-May mean extinction height of 1.99 km given by Koffi et al. (2012). However,
 321 model estimates of z_{α} in the control run are generally higher than those inferred from
 322 ground- and satellite-based data sets over different locations/areas in South Asia, as shown in
 323 Table 2. The only exception is the comparison with MPL data at Nainital, with a slightly
 324 lower model-calculated z_{α} . This might be due to spatial averaging differences between the
 325 12-km grid mean model results and the point-based MPL data, because the comparison of z_{α}
 326 with the value estimated from CALIPSO for Nainital points to model overestimation,
 327 consistent with the other sites. The analysis of extinction profiles confirms model
 328 underestimation of column AOD in March and moreover, indicates that the low bias in AOD
 329 arises mainly from calculated lower aerosol burden in the lower atmosphere, which leads to
 330 an AOD underestimate of $> 50\%$, irrespective of location. These differences between the
 331 observed and modeled profiles at low altitudes are generally larger than the uncertainties
 332 associated with ground-based measurements (~40%). Although the CALIPSO satellite
 333 retrievals indicate uncertainties of ~91% to 110%, at the two ground sites their monthly mean
 334 values are comparable with the ground-based measurements. This validation provides support

335 to the regional mean comparison with the CALIPSO data here, as no sufficient ground-based
336 measurements are available on the regional scale. Comparison of the standard deviations in
337 the daily extinction profiles (Fig. S3 in the Supplement) and two-sample t-test of daily
338 aerosol extinction time series suggest that the differences between the model calculations and
339 observations (MPL data for Nainital and Kanpur; and CALIPSO data for South Asia) are
340 significant below 2.5 km with p-values less than the significance level of 0.05 (in the
341 Supplement).

342 To examine potential impacts on calculated radiative and thermodynamic processes from
343 the underestimation of aerosols, sensitivity model runs are conducted for March 2012 by
344 optimizing matching of the observed aerosol vertical profiles. The calculated aerosol
345 extinctions in the lowest eight model layers (below ~850 hPa, at 1.5-3 km above sea level in
346 the simulated model domain) are increased by a factor of 2 at each time step to reduce the
347 identified low bias. However, there are no independent observations of aerosol absorption
348 vertical profiles to constrain the model. AERONET SSA or the satellite-based absorption
349 AOD retrievals provide constraints for column-integrated absorption properties, but neither
350 of them resolves in altitude. To address this uncertainty, two approaches are tested for
351 adjusting the extinction profiles. In Case I, the calculated scattering and absorption
352 coefficients are increased proportionally, so that the altitude-dependent SSA — the fraction of
353 scattering in total extinction — remains the same as in the control run. This case assumes that
354 the underestimation of AOD is contributed proportionally by both scattering and absorbing
355 aerosol loadings. In Case II, only the calculated aerosol scattering coefficient is increased to
356 compensate for the AOD underpredictions, whereas the absorption coefficient remains the
357 same as in the control run, so that the aerosol SSA is increased. This assumption for example
358 could represent for a case study of the underrepresented hygroscopic growth of aerosol
359 particles postulated in other studies for this region (Pan et al., 2015). Comparing Cases I and
360 II will help to illuminate the impact due to uncertainty in modeled aerosol absorption profiles,
361 when the model representation of aerosol extinction profiles is comparable to observations.

362 As Fig. 1c shows, the zonal-mean AOD comparison with the MODIS observations as a
363 function of latitude is much improved in the sensitivity studies with the adjusted extinction
364 profiles (red dot-dashed line). The domain-averaged mean AOD is higher at 0.31 compared to

365 the base case value of 0.12, and only about 11% lower than that obtained from the MODIS
366 retrieval (0.35). Similarly, adjustment of the extinction profiles also leads to significant
367 improvement in the comparison with MPL and CALIPSO vertical profiles (Fig. 2 and Table
368 1). Below 850 hPa, the average percentage differences from the CALIPSO extinction profiles
369 decrease to -12%, -11%, and -30% at Nainital, Kanpur, and South Asia, respectively. The
370 mean errors averaged through the entire column also decrease to -22%, -14%, and -40%,
371 respectively.

372 Some of the remaining differences between the calculated and observed profiles in the
373 sensitivity studies can be attributed to uncertainty associated with column AOD retrievals by
374 CALIPSO. When the CALIPSO extinction profiles are normalized to the MODIS AOD data,
375 the differences between modeled and observed extinction profiles averaged over the South
376 Asia domain (Figs. 2c and 2f) are decreased to -16% for the entire column and -0.4% below
377 850 hPa (Table 1). This confirms that the bias correction method introduced in the sensitivity
378 studies compares better with the observed extinction profiles on the regional scale. On the
379 other hand, the CALIPSO profile normalized to the column integral of the MPL-retrieved
380 extinctions at Kanpur results in even larger AOD, thus enlarging the discrepancy from the
381 predicted extinction profile to -33%. At Nainital, normalization makes little difference,
382 because the surface and satellite retrievals of column AOD agree well at this site. Overall, at
383 both ground sites and on the regional mean, the simulations of aerosol extinctions,
384 particularly near the surface (below 2-3 km), are significantly improved in the sensitivity
385 studies, compared to the control run. Furthermore, Table 2 shows that, for various regions in
386 South Asia, the estimated mean extinction height z_α for the adjusted extinction profiles in
387 the sensitivity studies is generally lowered by about 10-20%. This also results in better
388 agreement with the CALIPSO-inferred mean extinction heights. In the sections below,
389 radiative and thermodynamic responses to these improved aerosol extinction profiles are
390 discussed.

391 **3.3 Radiative and surface temperature responses**

392 The buildup of aerosols in March plays an important role in modulating the distribution
393 of solar radiation throughout the atmosphere over South Asia. In the control run, the
394 aerosol-induced change in net downward solar radiation at the TOA is estimated at about -3

395 W m^{-2} , averaged over South Asia (Table 3), suggesting an overall cooling effect. On the other
396 hand, aerosols heat the atmosphere by absorbing incoming solar radiation at $+6.3 \text{ W m}^{-2}$. This
397 reduces the net downward radiation at the surface (surface dimming) by -9.3 W m^{-2} . These
398 estimated changes in radiation fluxes not only account for the instantaneous perturbation on
399 radiation by aerosols (aerosol direct radiative forcing), but they also include the effects of
400 rapid responses to aerosols at the land surface and in clouds (semi-direct radiative effects).
401 Because aerosol extinctions (thus AODs) in Cases I and II are increased to the same level, the
402 TOA radiative effects of aerosols are similar for the two cases, a net reduction of about -5 W
403 m^{-2} . However, the distribution of incoming solar (shortwave) radiation in the column is very
404 different between the two cases: the estimated atmospheric absorption is 50% stronger in
405 Case I, leading to a larger negative aerosol forcing at the surface (-14.2 W m^{-2}) than in Case II
406 (-11.7 W m^{-2}).

407 The aerosol impact on the surface air temperature (at 2 m) in the model simulations,
408 linked directly to aerosols' perturbation of the radiation budget, is shown in Fig. 3 as a
409 function of latitude over the land and oceans, respectively. Because the sea surface
410 temperature is fixed, the surface air temperature over the ocean responds little to aerosol
411 surface forcing. The near-surface air temperature responds mainly to aerosol heating and
412 increases in the lower atmosphere over the ocean. . In contrast, the absolute changes in the
413 surface air temperature are much more significant over the land area, and they are also
414 opposite in sign. Over land, the dominating effect of aerosols is cooling corresponding to an
415 overall negative forcing at the TOA. The latitudinal variations in the surface air temperature
416 changes are consistent with the AOD distribution, with a maximum up to -0.45 K at around
417 26°N . Of the three simulations, Case II estimates the largest cooling by aerosols at the surface,
418 although the largest surface dimming of the incoming radiation is given by Case I (Table 3).
419 This could be because aerosols over land are generally concentrated near the surface, and the
420 aerosol-induced warming of the lower atmosphere offsets the cooling due to the surface
421 dimming (Penner et al., 2003). Because Case I has more absorbing aerosols, the near-surface
422 compensating heating effect is stronger, resulting in weaker surface cooling for the same
423 AOD conditions as in Case II. The breakdown of the heating rate changes due to individual
424 processes is discussed in the next section.

3.4 Lower-atmosphere heating rate response

In addition to instantaneous radiative heating due to aerosol absorption of solar radiation, rapid adjustments in the surface energy balance and BL dynamical and thermodynamical processes also influence the heating rate in the lower atmosphere. The heating rate in a volume of air or the temperature tendency term (dT/dt) is calculated in the WRF-Chem model as a function of altitude for five different physical processes: shortwave (SW) and longwave (LW) radiation, BL mixing, exchange of the latent heat flux in cloud microphysics (Micro), and heat transport in cumulus (deep convection) parameterization. The differences in the calculated heating rates with and without aerosols are shown in Fig. 4 for individual processes, except that cumulus cloud parameterization — a small term at a grid spacing of 12 km in March — is not shown. The heating rate profiles are shown separately over the land (Figs. 4a-c) and oceans (Figs. 4d-f). The land-ocean contrast is evident in SW heating rates that are much more significant over land because of higher aerosol loadings. The SW heating over the ocean peaks at more elevated levels, mostly above ~ 900 hPa, not as close to the surface as over the continental source regions. Since the sea surface temperature is fixed in the simulations, stronger lower-atmosphere thermodynamic responses (indicated by larger heating rates) are estimated over the land than over the ocean for BL and LW process.

Consistent with the atmospheric forcing shown in Table 3, Case I estimates the largest diurnal mean SW heating rate (maximum ~ 0.7 K/day) of the three cases, and the SW heating rate in Case II is similar to that for the control run (maximum ~ 0.35 K/day). Forced by the same aerosol extinction profiles with the bias correction, the differences in calculated heating rates for individual processes between Case I and Case II are shown in Fig. 4. These results demonstrate the impact of different absorbing aerosol profiles on boundary layer dynamics and cloud microphysics processes. The BL cooling is initiated as a dynamical response to both surface dimming and atmospheric heating by aerosols. Because the simulated aerosol effects reduce the temperature gradient between the land and atmosphere, the surface buoyancy production is reduced. It leads to the suppression of the convection in the BL that transports the heat fluxes, causing the cooling. Over land, the local maximum cooling due to BL mixing occurs at the height with the largest SW heating; the larger SW heating in Case I also drives stronger BL cooling than in Case II. The LW radiation responds similarly to

455 surface dimming and atmosphere heating, so Case I estimates the largest LW cooling over
456 land. Over the ocean, the LW responses are also affected by cloud microphysics processes
457 (i.e., the subsequent latent heat flux exchanges from cloud condensation and evaporation
458 [Micro]). Because absorbing aerosols tend to stabilize the lower atmosphere and suppress the
459 cloud formation, Case I estimates a smaller Micro heating rate at the cloud condensation level
460 and also a smaller LW heating (cooling) below (above) the cloud layer over the ocean than
461 Case II.

462 The total aerosol impact on the lower-atmosphere temperature profile is determined by
463 the combined effects of all the heating rates (solid black line in Fig. 4). Over the ocean, the
464 total heating rate is strongly governed by the SW heating. Thus, Case I calculates the most
465 significant atmospheric heating by aerosols, which warms most of the lower atmosphere
466 below 600 hPa. The maximum heating occurs below the level where the SW heating rate
467 peaks, because of compensating LW cooling by lower marine clouds. The heating response is
468 different over land. The calculated total heating rate deviates from the SW heating profile in
469 the lower atmosphere as a result of rapid thermodynamic adjustments over the land surface
470 and through BL mixing. Aerosols tend to have an overall cooling effect (negative heating rate)
471 near the surface that exceeds the direct instantaneous SW radiative heating. The surface
472 cooling rate is enhanced from ~ -0.4 K/day in the control run to -0.7 K/day in Case I and -0.8
473 K/day in Case II after aerosol extinctions are increased nearly to the observed levels.

474 Furthermore, sensitivity studies of unconstrained partitioning between absorbing and
475 scattering components of aerosols (Case I versus Case II) show that higher atmospheric
476 heating due to a larger absorption fraction (as in Case I) offsets part of the near-surface BL
477 and LW cooling responses generated, which are similar to those in Case II. Therefore, Case I
478 warms the lower atmosphere more pronouncedly than Case II but cools less at the land
479 surface. This implies that the manifestation of aerosol direct and semi-direct radiative effects
480 not only depends on the aerosol extinction profile but also is affected strongly by aerosol
481 absorption. These uncertainties in the estimated heating rates resulting from aerosol vertical
482 distributions further propagate into simulations of the BL height and cloudiness, as discussed
483 below.

484 **3.5 Atmospheric dynamic and thermodynamic responses**

485 As a result of changes in the heating rate, aerosol effects tend to stabilize the lower
486 atmosphere over land. As Fig. 5 shows, the predicted BL height is lowered over most of the
487 land areas in all three simulations compared to the run without aerosol-radiation feedbacks.
488 The reduction in the BL height is about -10% to -20% at locations where the estimated peak
489 BL height (at 1300-1400 local time) is above 2-3 km during the pre-monsoon month. The
490 aerosol impact on the BL height is more significant with increased AOD or extinction in the
491 sensitivity studies, Case I and Case II, than in the control run. Moreover, more absorbing
492 aerosols in Case I result in smaller reductions in the BL height than in Case II. This implies
493 that the BL height is predominately linked to surface cooling. Because Case II generates the
494 largest cooling at the surface (Fig. 3), we obtain the largest reductions in the BL heights for
495 Case II. On some portions of the ocean and land surfaces, the BL height is moderately higher
496 (roughly about 200 m) with aerosols, and these regions correspond to areas where aerosols
497 generally have a warming effect on the near-surface air temperature.

498 Figure 6 illustrates percent changes due to aerosols in meridional circulation (v , $-\omega$) and
499 total precipitable water vapor (background color map) averaged at 60-95°E. These changes
500 are linked closely to anomalies of total heating or cooling in the atmosphere (Fig. 4). At
501 5-20°N where ocean prevails, atmospheric heating by aerosols results in strengthening of the
502 upward motion in all three model simulations, especially below 700 hPa (Figs. 6a-c). This is
503 accompanied by enhanced large-scale subsidence in the lower troposphere north of 20°N
504 where land surface prevails and aerosols have an overall cooling effect due to strong negative
505 LW and BL responses. The largest enhancement in the ascending zone for aerosols is in Case
506 I, which also has the highest absorbing aerosol content. Similarly, Case II, with the strongest
507 cooling, calculates the largest enhancement in the descending zone.

508 The changes in updraft and downdraft are consistent with the aerosol-induced changes in
509 surface pressure, as illustrated in Fig. 6d for Case I. The decreased pressure over the ocean
510 and an increase over the northern Indian subcontinent are accompanied by enhanced
511 convergence at 850 hPa over the Arabian Sea and enhanced divergence over the eastern India
512 coast, adjacent to the Bay of Bengal. The high-pressure system and divergence drive
513 recirculation of the subsidence flow northward and form more terrain-elevated convection
514 along the Himalayan foothills. Aerosols transported over high-elevation mountains induce a

515 warming effect over the snow-covered surface by reducing the surface albedo, thus enhancing
516 convective updraft over the Qinghai–Tibet Plateau.

517 In response to the radiative and dynamical perturbation, the aerosol-induced
518 thermodynamic responses are manifested through enhanced surface evaporation and upward
519 transport of clean, moist marine air from the northern Indian Ocean (Figs. 6a-c). The
520 elevation of water vapor to the upper troposphere in the tropics leads to reduced moisture in
521 the middle troposphere over the subtropics. The calculated percent changes in predicted total
522 precipitable water vapor are very sensitive to the aerosol properties simulated. Compared
523 with the control run, Case I predicts both larger increases of water vapor at 5-20°N and larger
524 decreases of water vapor north of 20°N in the free troposphere, as a result of increased
525 aerosol extinctions and AOD. On the other hand, Case II has the same aerosol extinctions and
526 AOD as Case I but gives rise to weaker BL moistening in the tropics and stronger drying (by
527 about 50% drier than Case I) in the middle troposphere of the subtropics (>15°N), as a result
528 of less light-absorptive aerosols.

529 As for water vapor, Fig. 7 shows responses in cloudiness for different aerosol simulations.
530 Cloud frequency of occurrence is calculated as percent of hours in a month with non-zero
531 liquid water cloud fraction below 500 hPa in each column. In pre-monsoonal March, clouds
532 occur more frequently over the tropical and subtropical ocean than land, in the range of 20-80%
533 (green contour lines in Fig. 7). Over most of the land, cloud occurrence is lower than 10%,
534 except for the mountainous areas and over the Plateau with orographic and convective cloud
535 formation which is either not very susceptible to aerosol effects or has low aerosol
536 concentrations. Therefore, over the polluted land surface, in spite of high aerosol loadings,
537 cloud changes resulting from the simulated aerosol effects are small within $\pm 5\%$ and
538 considered as insignificant, as shown by the color map in Fig. 7a. The most significant cloud
539 response is found over the Bay of Bengal at 10-20°N, where the cloud occurrence exceeds 60%
540 of the time and aerosol loadings are also high. Increased aerosol extinctions in Case I (Fig. 7b)
541 and Case II (Fig. 7c) result in different cloud responses from the control run (Fig. 7a), which
542 calculates a moderate increase of 5-10% in cloudiness due to aerosols. Case I enhances the
543 aerosol effect in the control run and calculates a distinct and overwhelming increase of 10-20%
544 more cloudy skies over this region, whereas cloud formation in Case II is largely suppressed

545 and aerosols are found to decrease cloudiness by about 5-10% over some areas. Therefore,
546 while aerosol extinctions being the same, a smaller SSA (more absorbing aerosols) in Case I
547 could change the cloud response to aerosol radiative effects from negative to positive in
548 pre-monsoon month. And this uncertainty in cloud response up to 10-20% could contribute to
549 about one third of the calculated local cloud frequency of occurrence (40-60%).

550 **4. Summary and Discussion**

551 Although aerosol radiative effects have been incorporated into global and regional
552 climate simulations, quantification of simulated aerosol vertical distributions and subsequent
553 climate responses in large-scale models is lacking. This is of particular importance for
554 climate studies over South Asia, where high concentrations of aerosols are possibly linked to
555 weakening of the South Asian Monsoon in the 20th century (Bollasina et al., 2014). During
556 March 2012, ground-based lidar measurements of vertical distributions of aerosol extinctions
557 were made available in a polluted area of northern India, both at a high-elevation site
558 (Nainital) near the BL top and at a valley site (Kanpur) near sea level. The aerosol extinction
559 profiles retrieved at these two sites provide an independent ground calibration of CALIPSO
560 satellite retrievals of aerosol vertical distributions, which cover a more extended domain.
561 Together, the profiles are used to identify altitude-related bias in WRF-Chem regional model
562 simulations of aerosol optical properties over this region.

563 Our study reveals some broad tendencies and biases in model AOD simulations over
564 South Asia. Compared to the MODIS satellite AOD, the WRF-Chem model generally
565 underestimates AOD, despite using a high-resolution regional model with a grid spacing of
566 12 km and updated anthropogenic emissions. On a zonal or regional mean basis, the modeled
567 AODs are underestimated by about half of the MODIS retrievals. Furthermore, we
568 demonstrate that the low bias in column AOD is mainly associated with underprediction of
569 aerosol extinctions in the lower troposphere versus observed extinction profiles. Systematic
570 underestimation of > 50% was observed below 2-3 km at the two ground sites. Comparison
571 with CALIPSO satellite data indicates even larger discrepancies of roughly 77% below ~2
572 km on a regional mean basis, although some of the differences can be attributed to
573 uncertainty associated with the CALIPSO retrievals of column AOD. Above ~2 km, the
574 model's low bias in calculated aerosol extinction is smaller and the extent of the model

575 underestimation also varies depending on the geographical locations. Previous studies have
576 indicated similar low bias (to different extents) in modeled column AOD (Ganguly et al.,
577 2009; Cherian et al., 2013; Pan et al., 2015) and lower-atmosphere extinction coefficients (Yu
578 et al., 2010; Koffi et al., 2012; Pan et al., 2015) over this region. Therefore, although the
579 atmospheric radiative and dynamical responses derived from the sensitivity studies in this
580 study are based on the WRF-Chem model used in this study, the dependence on aerosol
581 extinction profiles might also be applicable to other model simulations.

582 Resolving the mismatch between simulated and observed aerosol extinction profiles
583 requires possible upgrades of multiple model physics schemes and quantification of key
584 parameters that could affect vertical distribution of aerosols, for instance, biomass burning
585 injection heights (Grell et al., 2011), boundary layer height and near-surface winds (Nair et al.,
586 2012). Additionally, high-quality measurements at different locations are also needed for
587 model evaluation over longer time periods, and it is recommended for future studies over this
588 region. Here, instead of speculating on factors that contribute to the model-data differences,
589 we apply a bias correction to simulated aerosol extinction profiles and demonstrate the
590 impact on regional climate simulations. In our sensitivity studies, increases in aerosol
591 extinction below 2-3 km lead to improved agreement in column AOD, from an
592 underestimation of -66% to -11% relative to MODIS retrievals averaged over South Asia.
593 This suggests that about 83% of the AOD underestimation is attributable to model levels
594 below 2-3 km. In addition, the column-mean differences between modeled and CALIPSO
595 extinction profiles averaged over the South Asia domain are reduced from 75% to 40% or 16%
596 if the CALIPSO profiles are normalized to the MODIS AOD retrievals. In the
597 aerosol-concentrated lower atmosphere below 2-3 km, the predicted regional-mean extinction
598 profile agrees with the CALIPSO retrieval within 30% or 0.4% compared with the CALIPSO
599 profile normalized to the MODIS AOD.

600 Compared to the control run, the increased aerosol extinctions in Case I and Case II
601 result in 63% and 80% larger negative forcing at the TOA for -4.9 and -5.4 W m^{-2} ,
602 respectively, and 53% and 26% stronger dimming effects at the surface for -14.2 and -11.7 W
603 m^{-2} , respectively. The contrast between Case I and Case II demonstrates the importance of
604 constraining the vertical distribution of aerosol absorption, in addition to extinction profiles.

605 When column AOD and extinction profiles are the same as in Case I and Case II, additional
606 absorbing aerosols (a smaller SSA) in Case I generate a 48% larger atmospheric forcing for
607 $+9.3 \text{ W m}^{-2}$.

608 More importantly, we demonstrate that the larger atmospheric heating and surface
609 dimming in Case I lead to smaller lower-atmosphere cooling (up to -0.7 K day^{-1}) over land
610 than in Case II (up to -0.8 K day^{-1}); in the latter, the aerosols cause a smaller energy
611 imbalance between the atmosphere and surface. This indicates that although absorbing
612 aerosols generate larger radiative heating in the atmosphere, they also cause stronger cooling
613 responses from the land surface and BL. These rapid adjustments counteract atmospheric
614 heating and lead to overall cooling at the surface and in the lower atmosphere. The resultant
615 cooling effect is lower than that due to fewer absorbing aerosols with the same AOD (a larger
616 SSA).

617 Consequently, atmospheric dynamic and thermodynamic processes also respond
618 differently. Case I predicts smaller reductions in BL height than Case II over land, as a result
619 of a more stabilized lower troposphere. On the other hand, the larger atmospheric warming
620 due to increased absorption of solar radiation in Case I increases surface evaporation from the
621 ocean and enhances the upward convective transport of moisture into the upper troposphere
622 in the tropics. The consequence is a reduction in the transport of moisture to the subtropical
623 lower-to-middle troposphere during the pre-monsoon time over this region. And clouds occur
624 more frequently over the Bay of Bengal. Although the simulated aerosol perturbation is small
625 for large-scale circulation (about 10 hPa day^{-1} vertically, and 0.1 m s^{-1} in the meridional
626 direction), water vapor ($\pm 6\%$), and cloud occurrence ($\pm 10\%$), the propagated uncertainty due
627 to aerosol extinction is comparable to the absolute aerosol effect, and the partitioning of
628 absorbing and scattering aerosols could change the sign of these responses.

629 In this work, we had to limit the evaluation of model vertical extinction profiles to one
630 month, because of the need for ground-based vertical profile observations at different
631 locations and times to validate and supplement the CALIPSO satellite retrievals. It would be
632 desirable to conduct similar evaluations for longer times and use ensemble members of
633 perturbed meteorological conditions to better investigate the climate response to uncertainties
634 in modeled aerosols. In addition, observational constraints on aerosol absorption profiles are

635 lacking. In particular, light absorption by brown carbon aerosols from biomass burning,
636 which are important aerosol sources in South Asia, might contribute additional aerosol
637 absorption (Feng et al., 2013). This absorption enhancement is not considered in this version
638 of the WRF-Chem model used for this study and evaluated. Also, model simulations of
639 semi-direct aerosol effects depend strongly on the model representation of clouds, which is
640 not examined here; on the other hand, cloud occurrences are generally low over this region
641 during the pre-monsoon month.

642 Nevertheless, this study improves the understanding of model underestimation of
643 aerosols in particular their vertical distribution over South Asia and highlights the importance
644 of accurate representation of both aerosol extinction and absorption profiles in regional
645 climate simulations. Determining whether aerosol scattering or absorption contributes to the
646 aerosol optical underestimation is critical, because the two sensitivity studies here reveal
647 different responses in predicted large-scale dynamics and in subsequent water vapor and
648 cloud distributions. Additional high-quality, routine measurements of both aerosol extinction
649 and absorption profiles are needed. Furthermore, we show that rapid adjustments in the land
650 surface energy budget and atmospheric dynamics modulate the instantaneous radiative
651 perturbation by aerosols with comparable force and can either amplify or offset the direct
652 aerosol radiative forcing. Our results thus reinforce the need for observational constraints of
653 effective radiative forcing, which includes both direct and semi-direct radiative effects, for
654 quantifying aerosol-radiation interactions, as suggested in the Intergovernmental Panel on
655 Climate Change fifth assessment report (Boucher et al., 2013).

656

657

658 **Acknowledgments.** This work was supported by the U.S. Department of Energy (DOE) as
659 part of the Atmospheric System Research Program. Support for this research was provided to
660 YF, VRK, RC, and MC by Argonne National Laboratory under U.S. DOE contract
661 DE-AC02-06CH11357. CZ's contribution to this study was supported by the U.S. DOE as
662 part of the Regional and Global Climate Modeling program through contract
663 DE-AC05-76RL01830. All of the numerical simulations were performed by using the
664 computing cluster (Fusion) operated by the Argonne's Laboratory Computing Resource

665 Center.

666

667 **References**

668

669 Ban-Weiss, G., L. Cao, G. Bala, and K. Caldeira: Dependence of climate forcing and
670 response on the altitude of black carbon aerosols. *Clim. Dyn.*, 38, 897–911, 2012.

671 Benjamin, S. G., G. A. Grell, J. M. Brown, and T. G. Smirnova: Mesoscale weather prediction
672 with the RUC hybrid isentropic-terrain-following coordinate model. *Mon. Wea. Rev.*, 132,
673 473-494, 2004.

674 Bollasina, M. A., Y. Ming, and V. Ramaswamy: Anthropogenic aerosols and the weakening of
675 the South Asian summer monsoon, *Science*, 334(6055), 502–505,
676 doi:10.1126/science.1204994, 2011.

677 Bollasina, M. A., Y. Ming, V. Ramaswamy, M. D. Schwarzkopf, and V. Naik: Contribution of
678 local and remote anthropogenic aerosols to the twentieth century weakening of the South
679 Asian Monsoon, *Geophys. Res. Lett.*, 41, 680–687, doi:10.1002/2013GL058183, 2014.

680 Boucher, O., D. Randall, P. Artaxo, C. Bretherton, G. Feingold, P. Forster, V.-M. Kerminen, Y.
681 Kondo, H. Liao, U. Lohmann, P. Rasch, S.K. Satheesh, S. Sherwood, B. Stevens and X.Y.
682 Zhang, Clouds and Aerosols. In: *Climate Change 2013: The Physical Science Basis.*
683 *Contribution of Working Group I to the Fifth Assessment Report of the*
684 *Intergovernmental Panel on Climate Change* [Stocker, T.F., D. Qin, G.-K. Plattner, M.
685 Tignor, S.K. Allen, J. Boschung, A. Nauels, Y. Xia, V. Bex and P.M. Midgley (eds.)].
686 Cambridge University Press, Cambridge, United Kingdom and New York, NY, USA,
687 2013.

688 Cherian, R., C. Venkataraman, J. Quaas, and S. Ramachandran: GCM simulations of
689 anthropogenic aerosol-induced changes in aerosol extinction, atmospheric heating and
690 precipitation over India, *J. Geophys. Res. Atmos.*, 118, 2938–2955,
691 doi:10.1002/jgrd.50298, 2013.

692 Chin, M., Ginoux, P., Kinne, S., Holben, B. N., Duncan, B. N., Martin, R. V., Logan, J. A.,
693 Higurashi, A., and Nakajima, T.: Tropospheric aerosol optical thickness from the
694 GOCART model and comparisons with satellite and sunphotometer measurements, *J.*
695 *Atmos. Sci.*, 59, 461–483, 2002.

696 Choi, J.-O., and C. E. Chung: Sensitivity of aerosol direct radiative forcing to aerosol vertical

697 profile, *Tellus B*, 66, 24376, <http://dx.doi.org/10.3402/tellusb.v66.24376>, 2014.

698 Chung, C. E., Ramanathan, V., Carmichael, G., Kulkarni, S., Tang, Y., Adhikary, B.,
699 Leung, L. R., and Qian, Y.: Anthropogenic aerosol radiative forcing in Asia derived from
700 regional models with atmospheric and aerosol data assimilation, *Atmos. Chem. Phys.*, 10,
701 6007-6024, doi:10.5194/acp-10-6007-2010, 2010.

702 Dey, S., and L. Di Girolamo: A climatology of aerosol optical and microphysical properties
703 over the Indian subcontinent from nine years (2000–2008) of Multiangle Imaging
704 SpectroRadiometer (MISR) data, *J. Geophys. Res.*, 115, D15204,
705 doi:10.1029/2009JD013395, 2010.

706 Eck, T. F., B. N. Holben, J. S. Reid, O. Dubovik, A. Smirnov, N. T. O’Neill, I. Slutsker, and S.
707 Kinne: Wavelength dependence of the optical depth of biomass burning, urban, and
708 desert dust aerosols, *J. Geophys. Res.*, 104, 31,333–31,349, doi:10.1029/1999JD900923,
709 1999.

710 Emmons, L. K., Walters, S., Hess, P. G., Lamarque, J.-F., Pfister, G. G., Fillmore, D., Granier,
711 C., Guenther, A., Kinnison, D., Laepple, T., Orlando, J., Tie, X., Tyndall, G., Wiedinmyer,
712 C., Baughcum, S. L., and Kloster, S.: Description and evaluation of the Model for Ozone
713 and Related chemical Tracers, version 4 (MOZART-4), *Geosci. Model Dev.*, 3, 43–67,
714 doi:10.5194/gmd-3-43-2010, 2010.

715 Fast, J. D, Gustafson Jr., W. I., Easter, R. C., Zaveri, R. A., Barnard, J. C., Chapman, E. G.,
716 and Grell, G. A.: Evolution of ozone, particulates, and aerosol direct forcing in an urban
717 area using a new fully-coupled meteorology, chemistry, and aerosol model, *J. Geophys.*
718 *Res.*, 111, D21305, doi:10.1029/2005JD006721, 2006.

719 Feng, Y., V. Ramanathan, and V. R. Kotamarthi, Brown Carbon: a Significant Atmospheric
720 Absorber of Solar Radiation? *Atmos. Chem. Phys. Discuss.*, 13, 2795-2833,
721 doi:10.5194/acpd-13-2795-2013, 2013.

722 Feng, Y., M. Cadetdu, V. R. Kotamarthi, R. Renju and C. Suresh Raju, Humidity Bias and
723 Effect on Simulated Aerosol Optical Properties during the Ganges Valley Experiment,
724 submitted to *Current Science*, in review, 2015.

725 Ganguly, D., P. Ginoux, V. Ramaswamy, D. M. Winker, B. N. Holben, and S. N. Tripathi:
726 Retrieving the composition and concentration of aerosols over the Indo-Gangetic basin

727 using CALIOP and AERONET data, *Geophys. Res. Lett.*, 36, L13806, doi:10.1029/
728 2009GL038315, 2009.

729 Ganguly, D., Rasch, P. J., Wang, H., and Yoon, J.: Climate response of the South Asian
730 monsoon system to anthropogenic aerosols, *J. Geophys. Res.*, 117, D13209, 15
731 doi:10.1029/2012JD017508, 2012.

732 Gautam, R., Hsu, N. C., and Lau, K.-M.: Premonsoon aerosol characterization and radiative
733 effects over the Indo-Gangetic Plains: Implications for regional climate warming, *J.*
734 *Geophys. Res.*, 115, D17208, doi:10.1029/2010JD013819, 2010.

735 Ginoux, P., Chin, M., Tegen, I., Prospero, J. M., Holben, B., Dubovik, O., and Lin, S. J.:
736 Sources and distributions of dust aerosols simulated with the GOCART model, *J.*
737 *Geophys. Res.- Atmos.*, 106, 20255–20273, 2001.

738 Grell, G. A., Peckham, S. E., Schmitz, R., McKeen, S. A., Frost, G., Skamarock, W. C., and
739 Eder, B.: Fully coupled “online” chemistry within the WRF model, *Atmos. Environ.*, 39,
740 6957–6975, 2005.

741 Grell, G., Freitas, S. R., Stuefer, M., and Fast, J.: Inclusion of biomass burning in WRF-Chem:
742 impact of wildfires on weather forecasts, *Atmos. Chem. Phys.*, 11, 5289-5303, 2011.

743 Haywood, J. M. and Shine, K. P.: Multi-spectral calculations of the direct radiative forcing of
744 tropospheric sulphate and soot aerosols using a column model. *Q. J. Roy. Meteorol. Soc.*,
745 123, 1907-1930, 1997.

746 Holben, B. N., Eck, T. F., Slutsker, I., et al.: AERONET – A federated instrument network and
747 data archive for aerosol characterization, *Rem. Sens. Environ.*, 66, 1–16, 1998.

748 Iacono, M. J., J. S. Delamere, E. J. Mlawer, M. W. Shephard, S. A. Clough, and W. D. Collins:
749 Radiative forcing by long-lived greenhouse gases: Calculations with the AER radiative
750 transfer models. *J. Geophys. Res.*, 113, D13103, 2008.

751 Jacob, D. J., Crawford, J. H., Maring, H., Clarke, A. D., Dibb, J. E., Emmons, L. K., Ferrare,
752 R. A., Hostetler, C. A., Russell, P. B., Singh, H. B., Thompson, A. M., Shaw, G. E.,
753 McCauley, E., Pederson, J. R., and Fisher, J. A.: The Arctic Research of the Composition
754 of the Troposphere from Aircraft and Satellites (ARCTAS) mission: design, execution,
755 and first results, *Atmos. Chem. Phys.*, 10, 5191–5212, doi:10.5194/acp-10-5191-2010,
756 2010.

757 Janjic, Z. I.: The Step–Mountain Eta Coordinate Model: Further developments of the
758 convection, viscous sublayer, and turbulence closure schemes. *Mon. Wea. Rev.*, 122,
759 927–945, 1994.

760 Kafle, D. N. and R. L. Coulter: Micropulse Lidar Derived Aerosol Optical Depth
761 Climatology at ARM Sites Worldwide, *J. Geophys. Res.*, 118, 13, 7293-7308, doi:
762 10.1002/jgrd.50536, 2013.

763 Kinne, S., et al.: An AeroCom initial assessment: optical properties in aerosol component
764 modules of global models. *Atmos. Chem. Phys.* 6, 1815–1834, 2006.

765 Klett, J. D.: Stable analytical inversion solution for processing lidar returns. *Applied Optics*,
766 Vol. 20, No. 2, pp211-220, Jan., 1981.

767 Koch, D., et al.: Evaluation of black carbon estimations in global aerosol models. *Atmos.*
768 *Chem. Phys.*, 9, 9001–9026, 2009.

769 Koffi, B., Schulz, M., Breon, F. M., Griesfeller, J., Winker, D., Balkanski, Y., Bauer, S.,
770 Berntsen, T., Chin, M. A., Collins, W. D., Dentener, F., Diehl, T., Easter, R., Ghan, S.,
771 Ginoux, P., Gong, S. L., Horowitz, L. W., Iversen, T., Kirkevåg, A., Koch, D., Krol, M.,
772 Myhre, G., Stier, P., and Takemura, T.: Application of the CALIOP layer product to
773 evaluate the vertical distribution of aerosols estimated by global models: Aero-Com
774 phase I results, *J. Geophys. Res.-Atmos.*, 117, D10201, doi:10.1029/2011jd016858, 2012.

775 Kuhlmann, J. and Quaas, J.: How can aerosols affect the Asian summer monsoon?
776 Assessment during three consecutive pre-monsoon seasons from CALIPSO satellite data,
777 *Atmos. Chem. Phys.*, 10, 4673-4688, doi:10.5194/acp-10-4673-2010, 2010.

778 Kumar, R., Barth, M. C., Madronich, S., Naja, M., Carmichael, G. R., Pfister, G. G., Knote,
779 C., Brasseur, G. P., Ojha, N., and Sarangi, T.: Effects of dust aerosols on tropospheric
780 chemistry during a typical pre-monsoon season dust storm in northern India, *Atmos.*
781 *Chem. Phys.*, 14, 6813–6834, 2014.

782 Lau, K. M., M. K. Kim, and K. M. Kim: Asian summer monsoon anomalies induced by
783 aerosol direct forcing: the role of the Tibetan Plateau, *Clim. Dyn.*, 26, 855-864, 2006.

784 Lau, K.-M., K.-M. Kim, C. N. Hsu, and B. N. Holben: Possible influences of air pollution,
785 dust- and sandstorms on the Indian monsoon, *WMO Bull.*, 58, 22–30, 2009.

786 Liao, H. and Seinfeld, J. H.: Effects of clouds on direct aerosol radiative forcing of climate, *J.*

787 *Geophys. Res.*, 103, 3781–3788, 1998.

788 Liu, X., et al.: Toward a minimal representation of aerosols in climate models: description
789 and evaluation in the Community Atmosphere Model CAM5, *Geosci. Model. Dev.*, 5,
790 709–739, 2012.

791 Loeb, N. G., and W. Y. Su: Direct aerosol radiative forcing uncertainty based on a radiative
792 perturbation analysis. *J. Clim.*, 23, 5288–5293, 2010.

793 Lohmann, U., and J. Feichter, Can the direct and semi-direct aerosol effect compete with the
794 indirect effect on a global scale? *Geophys. Res. Lett.*, 28, 159–161, 2001.

795 Lu Z, Zhang, Q. and Streets D. G.: Sulfur dioxide and primary carbonaceous aerosol
796 emissions in China and India 1996–2010, *Atmos. Chem. Phys.* 11 9839–9, 2011.

797 McComiskey, A., S. Schwartz, B. Schmid, H. Guan, E. Lewis, P. Ricchiazzi, and J. Ogren,
798 Direct aerosol forcing: Calculation from observables and sensitivities to inputs. *J.*
799 *Geophys. Res.*, 113, D09202, 2008.

800 Meehl, G. A., J. M. Arblaster, and W. D. Collins: Effects of black carbon aerosols on the
801 Indian monsoon, *J. Clim.*, 21, 2869–2882, doi:10.1175/2008JCLI2362.1, 2008.

802 Misra, A., S. N. Tripathi, D. S. Kaul, and E. J. Welton: Study of MPLNET-Derived Aerosol
803 Climatology over Kanpur, India, and Validation of CALIPSO Level 2 Version 3
804 Backscatter and Extinction Products. *J. Atmos. Oceanic Technol.*, 29, 1285–1294, 2012.

805 Moorthy, K. K., S. S. Babu, M. R. Manoj, and S. K. Satheesh: Buildup of aerosols over the
806 Indian Region, *Geophys. Res. Lett.*, 40, 1011–1014, doi:10.1002/grl.50165, 2013.

807 Myhre, G., Berglen, T. F., Johnsrud, M., Hoyle, C. R., Berntsen, T. K., Christopher, S. A.,
808 Fahey, D. W., Isaksen, I. S. A., Jones, T. A., Kahn, R. A., Loeb, N., Quinn, P., Remer, L.,
809 Schwarz, J. P., and Yttri, K. E.: Modelled radiative forcing of the direct aerosol effect
810 with multi-observation evaluation, *Atmos. Chem. Phys.*, 9, 1365–1392,
811 doi:10.5194/acp-9-1365-2009, 2009.

812 Myhre, G., et al.: Radiative forcing of the direct aerosol effect from AeroCom Phase II
813 simulations. *Atmos. Chem. Phys.*, 13, 1853–1877, 2013.

814 Nair, V. S., Solmon, F., Giorgi, F., Mariotti, L., Babu, S. S., and Moorthy, K. K.: Simulation
815 of South Asian aerosols for regional climate studies, *J. Geophys. Res.*, 117, D04209,
816 doi:10.1029/2011JD016711, 2012.

817

818 Pan, X., Chin, M., Gautam, R., Bian, H., Kim, D., Colarco, P. R., Diehl, T. L., Takemura, T.,
819 Pozzoli, L., Tsigaridis, K., Bauer, S., and Bellouin, N.: A multi-model evaluation of
820 aerosols over South Asia: common problems and possible causes, *Atmos. Chem. Phys.*,
821 15, 5903-5928, doi:10.5194/acp-15-5903-2015, 2015.

822 Penner, J.E., S.Y. Zhang, and C.C. Chuang: Soot and smoke aerosol may not warm climate. *J.*
823 *Geophys. Res.*, 108(D21), 4657, doi:10.1029/2003JD003409, 2003.

824 Petters, M. D. and Kreidenweis, S. M.: A single parameter representation of hygroscopic
825 growth and cloud condensation nucleus activity, *Atmos. Chem. Phys.*, 7, 1961-1971,
826 doi:10.5194/acp-7-1961-2007, 2007.

827 Pfister, G. G., Parrish, D. D., Worden, H., Emmons, L. K., Edwards, D. P., Wiedinmyer, C.,
828 Diskin, G. S., Huey, G., Oltmans, S. J., Thouret, V., Weinheimer, A., and Wisthaler, A.:
829 Characterizing summertime chemical boundary conditions for air masses entering the US
830 West Coast, *Atmos. Chem. Phys.*, 11, 1769–1790, doi:10.5194/acp-11-1769-2011, 2011.

831 Platnick, S., King, M. D., Ackerman, S. A., Menzel, W. P., Baum, B. A. and co-authors:
832 TheMODIS cloud products: algorithms and examples from Terra. *IEEE T Geosci.*
833 *Remote*, 41, 2, 459–473, 2003.

834 Quennehen, B., Raut, J.-C., Law, K. S., Ancellet, G., Clerbaux, C., Kim, S.-W., Lund, M. T.,
835 Myhre, G., Olivié, D. J. L., Safieddine, S., Skeie, R. B., Thomas, J. L., Tsyro, S.,
836 Bazureau, A., Bellouin, N., Daskalakis, N., Hu, M., Kanakidou, M., Klimont, Z.,
837 Kupiainen, K., Myriokefalitakis, S., Quaas, J., Rumbold, S. T., Schulz, M., Cherian, R.,
838 Shimizu, A., Wang, J., Yoon, S.-C., and Zhu, T.: Multi-model evaluation of short-lived
839 pollutant distributions over East Asia during summer 2008, *Atmos. Chem. Phys. Discuss.*,
840 15, 11049-11109, doi:10.5194/acpd-15-11049-2015, 2015.

841 Ramana, M. V., Ramanathan, V., Kim, D., Roberts, G. C., and Corrigan, C. E.: Albedo:
842 Atmospheric solar absorption and heating rate measurements with stacked UAVs, *Q. J.*
843 *Roy. Meteor. Soc.*, 133, 1913–1931, 2007.

844 Ramanathan, V., C. Chung, D. Kim, T. Bettge, L. Buja, J. T. Kiehl, W. M. Washington, Q. Fu,
845 D. R. Sikka, and M. Wild: Atmospheric brown clouds: Impacts on South Asian climate
846 and hydrological cycle, *P Natl Acad Sci USA*, 102(15), 5326-5333, 2005.

847 Ramanathan, V., et al.: Indian Ocean experiment: An integrated analysis of the climate
848 forcing and effects of the great Indo-Asian haze. *J. Geophys. Res.*, 106(D22), 28371–
849 28398, 2001

850 Ramanathan, V., M. V. Ramana, G. Roberts, D. Kim, C. Corrigan, C. Chung, and D. Winker:
851 Warming trends in Asia amplified by brown cloud solar absorption, *Nature*, 448, 575-578,
852 doi:10.1038/nature06019, 2007.

853 Samset, B. H., et al.: Black carbon vertical profiles strongly affect its radiative forcing
854 uncertainty, *Atmos. Chem. Phys.*, 13, 2423–2434, 2013.

855 Satheesh, S. K., K. K. Moorthy, S. S. Babu, V. Vinoj, and C. B. S. Dutt: Climate implications
856 of large warming by elevated aerosol over India, *Geophys. Res. Lett.*, 35, L19809,
857 doi:10.1029/2008GL034944, 2008.

858 Satheesh, S. K., K. K. Moorthy, S. S. Babu, V. Vinoj, V. S. Nair, S. N. Beegum, C. B. S. Dutt,
859 D. P. Alappattu, and P. K. Kunhikrishnan: Vertical structure and horizontal gradients of
860 aerosol extinction coefficients over coastal India inferred from airborne lidar
861 measurements during the Integrated Campaign for Aerosol, Gases and Radiation Budget
862 (ICARB) field campaign, *J. Geophys. Res.*, 114, D05204, doi:10.1029/2008JD011033,
863 2009.

864 Schmid, B., J. Michalsky, R. Halthore, M. Beauharnois, L. Harrison, J. Livingston, P. Russell,
865 B. Holben, T. Eck, and A. Smirnov: Comparison of aerosol optical depth from four solar
866 radiometers during the fall 1997 ARM intensive observation period, *Geophys. Res. Lett.*,
867 26, 2725 – 2728, doi:10.1029/1999GL900513, 1999.

868 Schwarz, J. P., et al.: Global-scale black carbon profiles observed in the remote atmosphere
869 and compared to models. *Geophys. Res. Lett.*, 37, L18812, 2010.

870 Shindell, D.T., J.-F. Lamarque, M. Schulz, M. Flanner, C. Jiao, M. Chin, P.J. Young, Y.H. Lee,
871 L. Rotstajn, N. Mahowald, G. Milly, G. Faluvegi, Y. Balkanski, W.J. Collins, A.J.
872 Conley, S. Dalsoren, R. Easter, S. Ghan, L. Horowitz, X. Liu, G. Myhre, T. Nagashima,
873 V. Naik, S.T. Rumbold, R. Skeie, K. Sudo, S. Szopa, T. Takemura, A. Voulgarakis, J.-H.
874 Yoon, and F. Lo: Radiative forcing in the ACCMIP historical and future climate
875 simulations. *Atmos. Chem. Phys.*, 13, 2939-2974, doi:10.5194/acp-13-2939-2013, 2013.

876 Skamarock, W. C., Klemp, J. B., Dudhia, J., Gill, D. O., Barker, D. M., Wang, W., and Powers,

877 J. G.: A description of the advancedresearch WRF version 2, NCAR Tech. Note,
878 NCAR/TN- 468+STR, Natl. Cent. for Atmos. Res., Boulder, Colo, available at:
879 <http://wrf-model.org/wrfadmin/publications.php>, 2008.

880 Smirnov, A., B. N. Holben, T. F. Eck, O. Dubovik, and I. Slutsker: Cloud screening and
881 quality control algorithms for the AERONET data base, *Remote Sens. Environ.*, 73, 337–
882 349, 2000.

883 Thompson, G., P. R. Field, R. M. Rasmussen, and W. D. Hall: Explicit Forecasts of Winter
884 Precipitation Using an Improved Bulk Microphysics Scheme. Part II: Implementation of
885 a New Snow Parameterization, *Mon. Wea. Rev.*, 136, 5095–5115, 2008.

886 Vuolo, M. R., Schulz, M., Balkanski, Y., and Takemura, T.: A new method for evaluating the
887 impact of vertical distribution on aerosol radiative forcing in general circulation models,
888 *Atmos. Chem. Phys.*, 14, 877-897, doi:10.5194/acp-14-877-2014, 2014.

889 Wang, C., D. Kim, A. M. L. Ekman, M. C. Barth, and P. J. Rasch: Impact of anthropogenic
890 aerosols on Indian summer monsoon, *Geophys. Res. Lett.*, 36, L21704,
891 doi:10.1029/2009GL040114, 2009.

892 Welton, E. J., and J. R. Campbell: Micropulse lidar signals: Uncertainty analysis. *J. Atmos.*
893 *Oceanic Technol.*, 19, 2089–2094, 2002.

894 Welton, E. J., J. R. Campbell, J. D. Spinhirne, and V. S. Scott III: Global monitoring of clouds
895 and aerosols using a network of micropulse lidar systems. *Lidar Remote Sensing for*
896 *Industry and Environment Monitoring*, U. N. Singh, Ed., International Society for
897 Optical Engineering (SPIE Proceedings, Vol. 4153), 151–158, doi:10.1117/12.417040,
898 2001.

899 Winker, D. M., Vaughan, M. A., Omar, A. H., Hu, Y., Powell, K. A., Liu, Z., Hunt, W. H., and
900 Young, S. A.: Overview of the CALIPSO Mission and CALIOP Data Processing
901 Algorithms, *J. Atmos. Oceanic Technol.*, 26, 2310–2323, 2009.

902 Yevich, R., and J. A. Logan: An assessment of biofuel use and burning of agricultural waste
903 in the developing world, *Global Biogeochem. Cycles*, 17(4), 1095,
904 doi:10.1029/2002GB001952, 2003.

905 Yu, H. B., M. Chin, D. M. Winker, A. H. Omar, Z. Y. Liu, C. Kittaka, and T. Diehl: Global
906 view of aerosol vertical distributions from CALIPSO lidar measurements and GOCART

907 simulations: Regional and seasonal variations. *J. Geophys. Res.*, 115, D00H30, 2010.

908 Yu, H., R. E. Dickinson, M. Chin, Y. J. Kaufman, B. N. Holben, I. V. Geogdzhayev, and M. I.
909 Mishchenko: Annual cycle of global distributions of aerosol optical depth from
910 integration of MODIS retrievals and GOCART model simulations, *J. Geophys. Res.*,
911 108(D3), 4128, doi:10.1029/2002JD002717, 2003.

912 Zarzycki, C. M. and Bond, T. C.: How much can the vertical distribution of black carbon
913 affect its global direct radiative forcing? *Geophys. Res. Lett.*, 37, L20807,
914 doi:10.1029/2010gl044555, 2010.

915 Zhang, G. J., and N. A. McFarlane: Sensitivity of climate simulations to the parameterization
916 of cumulus convection in the Canadian Climate Centre general circulation model.
917 *Atmos.– Ocean*, 33, 407–446, 1995.

918 Zhao, C., X. Liu, L. L. Ruby, and S. Hagos: Radiative impact of mineral dust on monsoon
919 precipitation variability over West Africa, *Atmos. Chem. Phys.*, 11:1879–1893, 2011.

920

921

922 **Tables**923 **Table 1.** Estimated differences relative to CALIPSO extinction profiles at Nainital, Kanpur,
924 and South Asia in March 2012

Site	Column Differences (%)			Differences below 850 hPa (%)		
	Model (control run)	Model (increased extinction)	Model (increased extinction)*	Model (control run)	Model (increased extinction)	Model (increased extinction)*
Nainital	-33	-22	-25	-56	-12	-16
Kanpur	-33	-14	-33	-52	-11	-31
S. Asia	-75	-40	-16	-77	-30	-0.4

925 *Percent differences relative to the CALIPSO extinction profiles normalized to the column
926 AOD inferred from the surface measurements for Nainital and Kanpur and the MODIS data
927 for South Asia.

928

929

930 **Table 2.** Calculated mean extinction height (km) from observations (MPL and CALIPSO)
931 and model simulations over different regions in March 2012

	Calculated Mean Extinction Height (km)					
	Nainital	Kanpur	Indo-Ganges basin	Central India	North Indian Ocean	South Asia
MPL	4.11	1.39	-	-	-	-
CALIPSO*	3.55 (3)	1.48 (4)	1.53 (9)	1.74 (4)	1.09 (5)	1.70 (29)
Model (control run)	4.00	2.09	1.86	1.91	1.73	1.85
Model (increased extinction)	3.64	1.68	1.69	1.68	1.53	1.68

932 *Numbers in the parentheses are the counts of CALIPSO tracks of the month.

933

934 **Table 3.** Aerosol-induced changes in shortwave radiation flux calculated by the WRF-Chem
935 model in the control run and two sensitivity studies (Case I and Case II) for March 2012,
936 averaged for 60-95°E, and 0-36°N.

	Aerosol-Induced Change ($W m^{-2}$)		
	Control run	Case I	Case II
Top of the atmosphere	-3.0	-4.9	-5.4
Atmosphere	+6.3	+9.3	+6.3
Surface	-9.3	-14.2	-11.7

937

938

939

940 **Figures**

941 **Figure 1.** For March 2012: (a) MODIS-retrieved and (b) simulated monthly mean AOD
942 distributions over South Asia. The locations of Nainital and Kanpur sites are indicated by red
943 dots. (c) Latitudinal variations in AOD averaged for 60-95°E from the model control run (red
944 solid), sensitivity runs (red dotted dash), and MODIS retrievals (blue). North of 27°N, more
945 than 2/3 of the MODIS AODs are missing (data not shown). (d) Comparison of simulated and
946 observed daily mean AOD at Nainital and Kanpur

947 **Figure 2.** Comparisons of monthly mean aerosol extinction profiles from model calculations
948 at 550nm (red squares for the control run and green open circles for the sensitivity studies),
949 ground-based MPL data at 532nm (solid black), satellite-retrieved CALIPSO data at 532nm
950 (dashed black), and CALIPSO data normalized to the MODIS AODs (dashed blue) (a) at
951 Nainital, (b) at Kanpur, and (c) over South Asia (60-95°E, 0-30°N), respectively. The
952 column-mean uncertainty in CALIPSO extinction data is $\pm 110\%$, $\pm 93\%$, and $\pm 91\%$ in panels
953 (a)-(c); Percent differences between the simulated and CALIPSO profiles are shown for (d)
954 Nainital, (e) Kanpur, and (f) South Asia

955 **Figure 3.** Changes in surface air temperature (K) due to aerosol radiative effects for three
956 model simulations

957 **Figure 4.** Calculated monthly mean heating rates (temperature tendency, dT/dt , in K/day)
958 perturbed by aerosols, over land for (a) the control run, (b) Case I, and (c) Case II, as well as
959 over the ocean for (d) the control run, (e) Case I, and (f) Case II. The heating processes
960 include shortwave (SW) radiation (red), longwave (LW) radiation (blue dashed), boundary
961 mixing (BL; magenta dashed), and cloud microphysics (Micro; green). The total heating due
962 to aerosol effects is shown with solid black lines

963 **Figure 5.** (a) Calculated monthly mean planetary BL height (PBLH) at 1300-1400 local time
964 for March, without aerosols; and estimated changes in PBLH ($\Delta PBLH$) due to aerosols in (b)
965 the control run, (c) Case I, and (d) Case II

966 **Figure 6.** Changes in meridional circulation (v , $-\omega$), averaged at 60-95°E, due to different
967 aerosol effects for (a) the control run, (b) Case I, and (c) Case II, where v (scaled to 0.1 m/s)
968 is the meridional velocity, and $-\omega$ (scaled to 10 hPa/day) is the vertical velocity. The
969 color-shaded contours in the background indicate the changes (%) in total precipitable water
970 (ΔQ_v) in the column due to aerosols. Panel (d) shows the changes in horizontal winds (u , v)
971 at 850 hPa and surface pressure changes (ΔPS_{SURF}) due to aerosols for Case I

972 **Figure 7.** Changes in frequency of cloud occurrence (defined as % of hours in a month with
973 clouds below 500hPa in each column) due to aerosols for (a) the control run, (b) Case I, and
974 (c) Case II. The contour lines in green color in each panel indicate calculated frequency of
975 cloud occurrence without aerosols. The contour levels are shown for 10%, 20%, 40%, and
976 60%

977

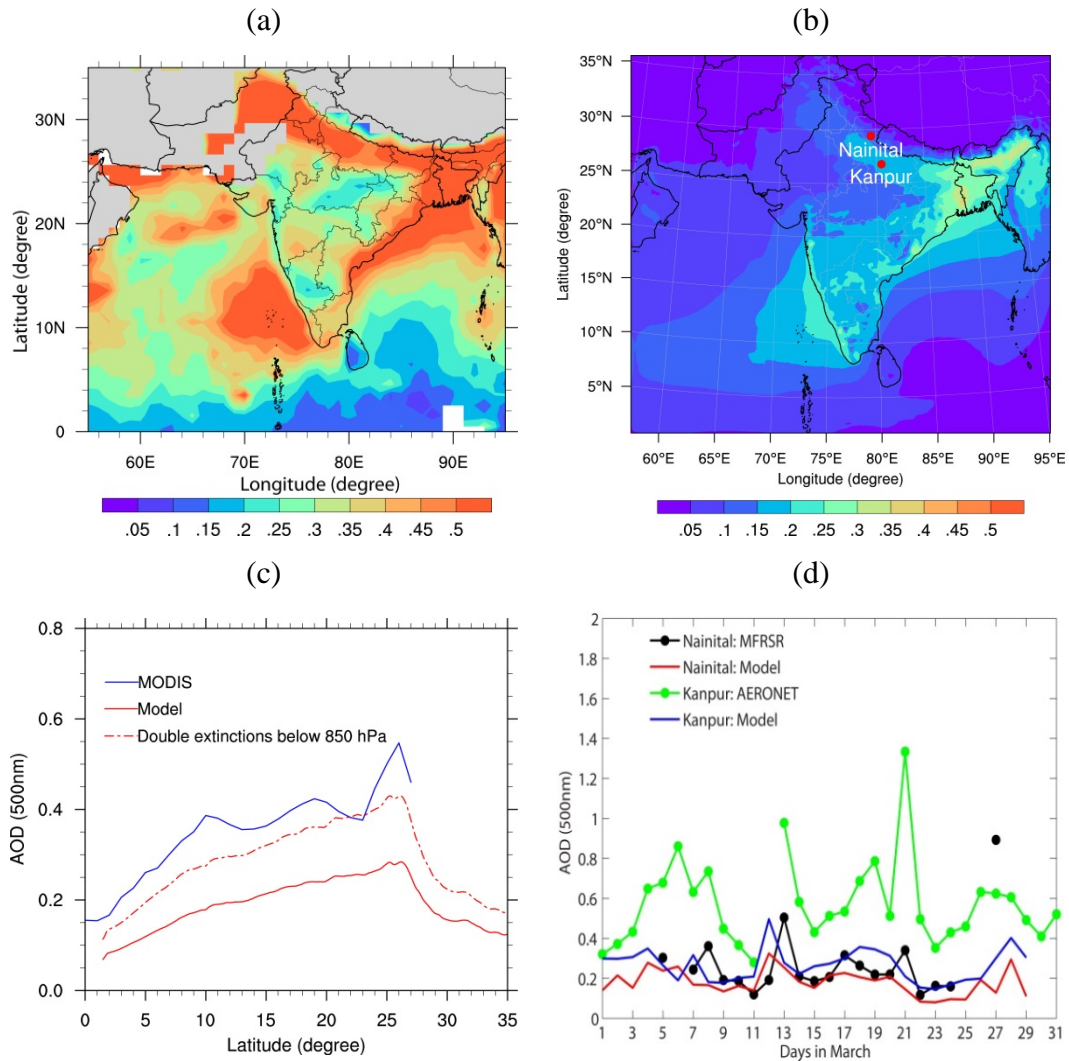


Figure 1. For March 2012: (a) MODIS-retrieved and (b) simulated monthly mean AOD distributions over South Asia. The locations of Nainital and Kanpur sites are indicated by red dots. (c) Latitudinal variations in AOD averaged for 60-95°E from the model control run (red solid), sensitivity run (red dotted dash), and MODIS retrievals (blue). North of 27°N, more than 2/3 of the MODIS AODs are missing (data not shown). (d) Comparison of simulated and observed daily mean AOD at Nainital and Kanpur

978

979

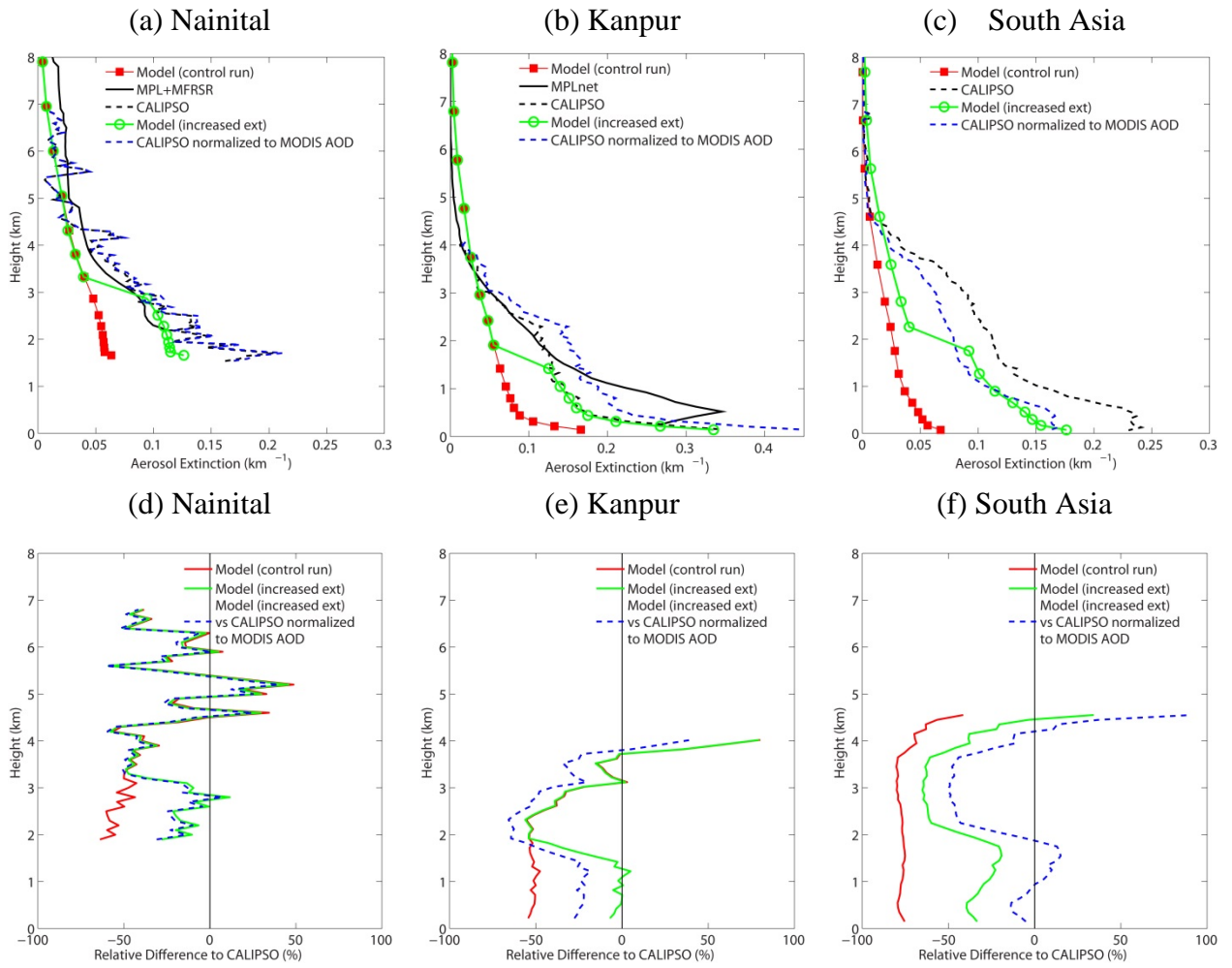


Figure 2. Comparisons of monthly mean aerosol extinction profiles from model calculations at 550nm (red squares for the control run and green open circles for the sensitivity studies), ground-based MPL data at 532nm (solid black), satellite-retrieved CALIPSO data at 532nm (dashed black), and CALIPSO data normalized to the MODIS AODs (dashed blue) (a) at Nainital, (b) at Kanpur, and (c) over South Asia (60-95°E, 0-30°N), respectively. The column-mean uncertainty in CALIPSO extinction data is $\pm 110\%$, $\pm 93\%$, and $\pm 91\%$ in panels (a)-(c); Percent differences between the simulated and CALIPSO profiles are shown for (d) Nainital, (e) Kanpur, and (f) South Asia.

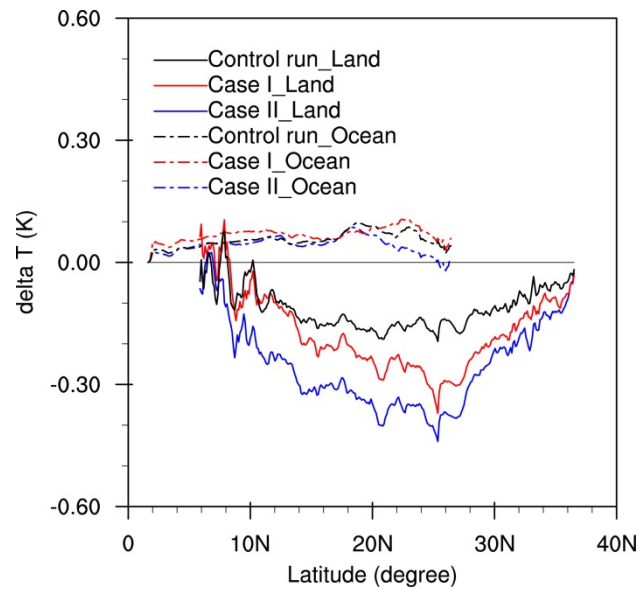


Figure 3. Changes in surface air temperature (K) due to aerosol radiative effects for three model simulations.

982

983

984

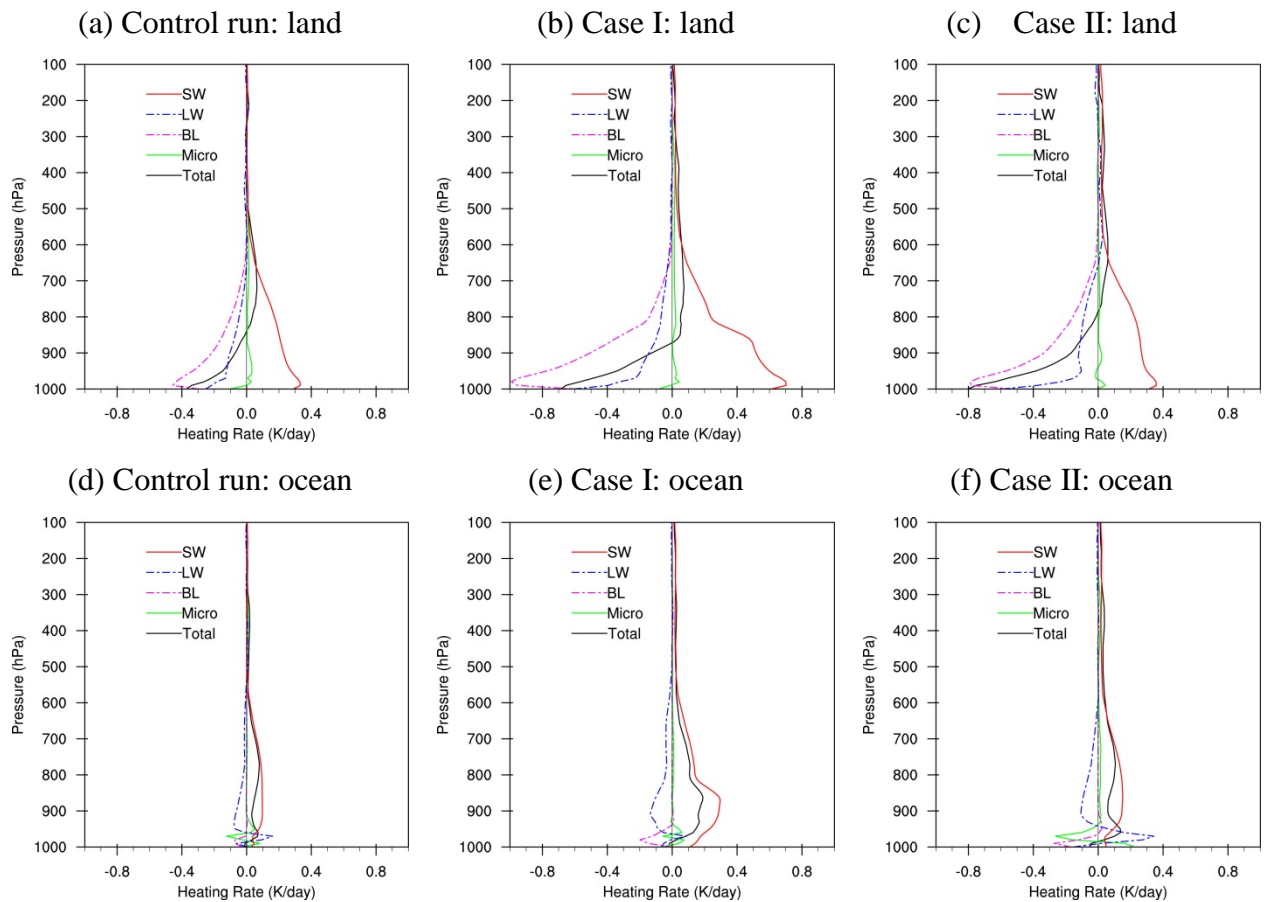


Figure 4. Calculated monthly mean heating rates (temperature tendency, dT/dt , in K/day) perturbed by aerosols, over land for (a) the control run, (b) Case I, and (c) Case II, as well as over the ocean for (d) the control run, (e) Case I, and (f) Case II. The heating processes include shortwave (SW) radiation (red), longwave (LW) radiation (blue dashed), boundary mixing (BL; magenta dashed), and cloud microphysics (Micro; green). The total heating due to aerosol effects is shown with solid black lines.

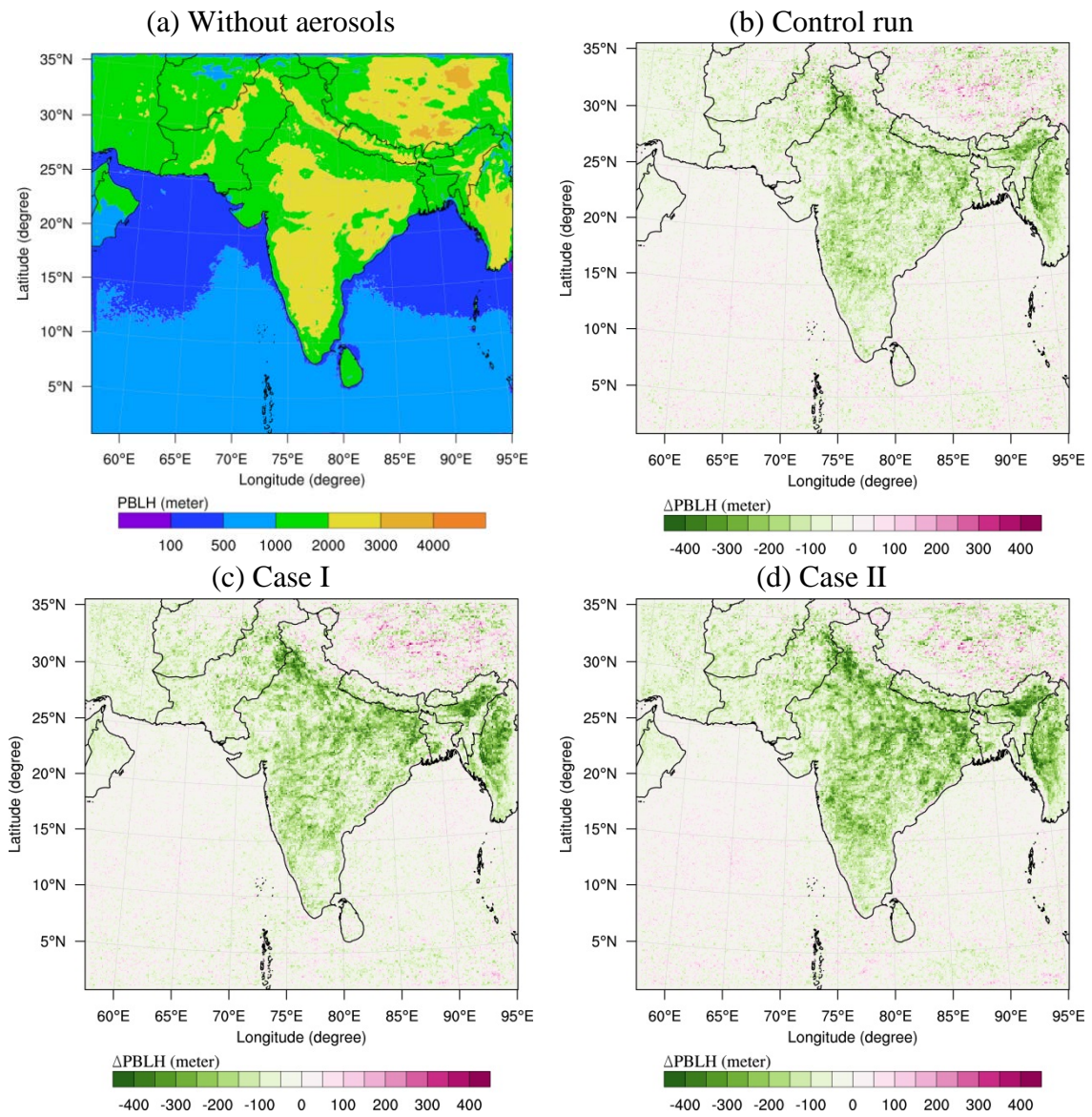


Figure 5. (a) Calculated monthly mean planetary BL height (PBLH) at 1300-1400 local time for March, without aerosols; and estimated changes in PBLH (Δ PBLH) due to aerosols in (b) the control run, (c) Case I, and (d) Case II.

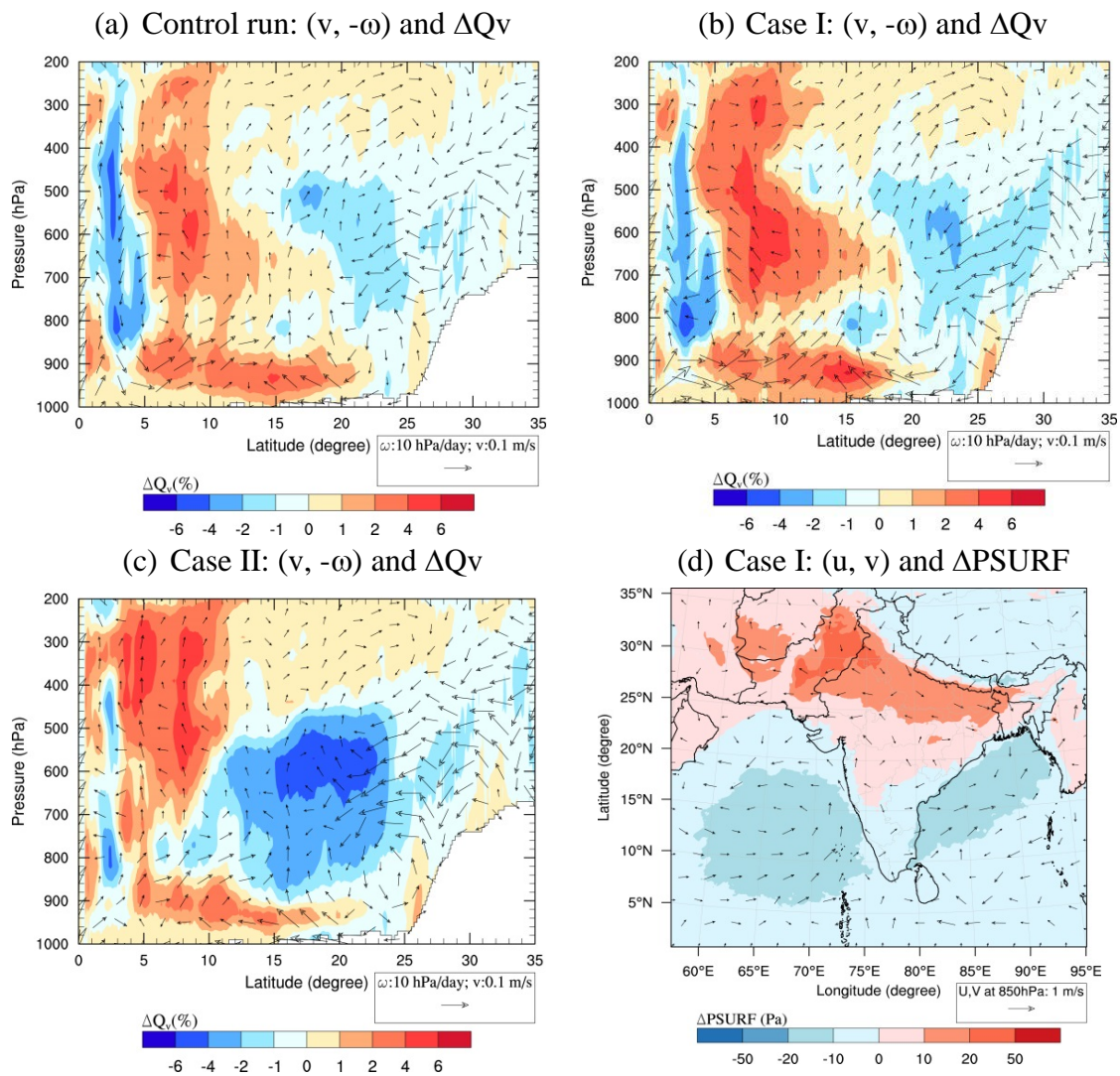


Figure 6. Changes in meridional circulation ($v, -\omega$), averaged at 60-95°E, due to different aerosol effects for (a) the control run, (b) Case I, and (c) Case II, where v (scaled to 0.1 m/s) is the meridional velocity, and $-\omega$ (scaled to 10 hPa/day) is the vertical velocity. The color-shaded contours in the background indicate the changes (%) in total precipitable water (ΔQ_v) in the column due to aerosols. Panel (d) shows the changes in horizontal winds (u, v) at 850 hPa and surface pressure changes ($\Delta PSURF$) due to aerosols for Case I.

992

993

994

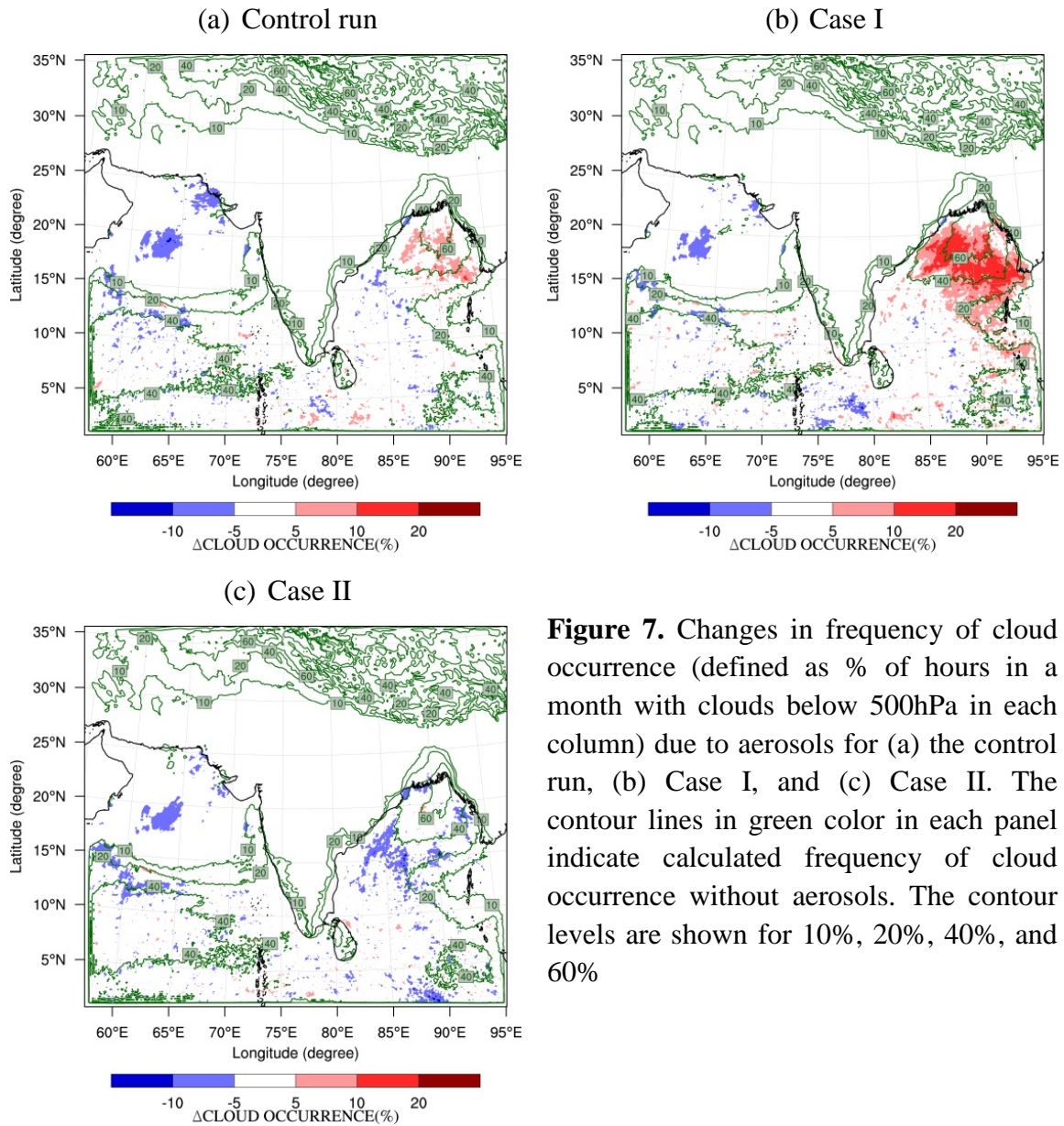


Figure 7. Changes in frequency of cloud occurrence (defined as % of hours in a month with clouds below 500hPa in each column) due to aerosols for (a) the control run, (b) Case I, and (c) Case II. The contour lines in green color in each panel indicate calculated frequency of cloud occurrence without aerosols. The contour levels are shown for 10%, 20%, 40%, and 60%